FORCE TECHNOLOGY

Project No. and Title of Report:

DMI 2000890.04

Development and Validation of Computational Ship Hydrodynamics

ONR Grant N00014-00-1-0589 Final Technical Report

DISTRIBUTION STATEMENT A
Approved for Public Release
Distribution Unlimited

20030915 095

Client: ONR	***Client's Ref.:***
Author(s): John Cross-Whiter, Claus Simonsen	***Date:*** 29-08-03 ***Approved by:*** Christo Cattle

Revision	Description	By	Checked	Approved	Date
0		JCW/ CDS		CRS	29-08-03

Keywords:	***Classification:*** ☐ **Open** ☐ **Internal** ☐ **Confidential**

GTS GODKENDT TEKNOLOGISK SERVICE

FORCE Technology, Kgs. Lyngby
Hjortekærsvej 99
2800 Kgs. Lyngby, Denmark
Tel. +45 72 15 77 00
Fax +45 72 15 77 01

FORCE Technology, Main office
Park Allé 345
2605 Brøndby, Denmark
Tel. +45 43 26 70 00
Fax +45 43 26 70 11
e-mail force@force.dk
www.force.dk

FORCE Technology Sweden AB
Tallmätargatan 7
721 34 Västerås, Sweden
Tel. +46 (0)21 490 30 00
Fax +46 (0)21 490 30 01
e-mail info@forcetechnology.se
www.forcetechnology.se

REPORT DOCUMENTATION PAGE

Form Approved
OMB No. 0704-0188

1. REPORT DATE (DD-MM-YYYY)	2. REPORT DATE	3. DATES COVERED (From - To)
29-08-2003	FINAL	01-05-2000 TO 31-05-2003

4. TITLE AND SUBTITLE
DEVELOPMENT AND VALIDATION OF COMPUTATIONAL SHIP HYDRODYNAMICS

5a. CONTRACT NUMBER

5b. GRANT NUMBER
N-00014-00-1-0589

5c. PROGRAM ELEMENT NUMBER

6. AUTHOR(S)
JOHN CROSS-WHITER
CLAUS SIMONSEN

5d. PROJECT NUMBER

5e. TASK NUMBER

5f. WORK UNIT NUMBER

7. PERFORMING ORGANIZATION NAME(S) AND ADDRESS(ES)
FORCE TECHNOLOGY
HJORTEKAERSVEJ 99
2800 LYNGBY
DENMARK

8. PERFORMING ORGANIZATION REPORT NUMBER
2000890-04

9. SPONSORING/MONITORING AGENCY NAME(S) AND ADDRESS(ES)
OFFICE OF NAVAL RESEARCH
BALLSTON CENTRE TOWER ONE
800 NORTH QUINCY STREET
ALLINGTON, VA 22217-5660

10. SPONSOR/MONITOR'S ACRONYM(S)
ONR

11. SPONSORING/MONITORING AGENCY REPORT NUMBER

12. DISTRIBUTION AVAILABILITY STATEMENT
APPROVED FOR PUBLIC RELEASE, DISTRIBUTION UNLIMITED

13. SUPPLEMENTARY NOTES

14. ABSTRACT
A DETAILED COMPUTATIONAL STUDY IS PRESENTED OF THE FORCES AND FLOW FIELDS ON THE TANKER 'ESSO OSAKA' IN SIMPLE MANOEUVRING CONDITIONS: 'STRAIGHT AHEAD' 'STATIC RUDDER' AND 'PURE DRIFT' THE GENERAL PURPOSE CODE CFDSHIP-IOWA IS USED. THE FREE SURFACE IS NEGLECTED, AND THE TWO EQUATION K-ω TURBULENCE MODEL IS USED. PROPELLER FORCES ARE APPLIED AS DISTRIBUTED BODY FORCES, DERIVED FROM POTENTIAL FLOW PROPELLER CALCULATIONS. THE RESULTS ARE RIGOROUSLY VERIFIED AND VALIDATED AGAINST EXPERIMENTAL DATA FROM PMM AND PIV TESTS

15. SUBJECT TERMS
CFD, RANS, VISCOUS-INVISCID INTERACTION, VERIFICATION, VALIDATION

16. SECURITY CLASSIFICATION OF:			17. LIMITATION OF ABSTRACT	18. NUMBER OF PAGES	19a. NAME OF RESPONSIBLE PERSON
a. REPORT	b. ABSTRACT	c. THIS PAGE			JOHN CROSS-WHITER
U	U	U	SAR	64	19b. TELEPONE NUMBER (Include area code) +45 7215 7740

LIST OF CONTENTS: **PAGE:**

1. Technical Objectives

1.1. Global objectives and motivation for project

As outlined in the grant proposal for the current project, Reference /1/, the overall technical objective for the current project was to investigate the manoeuvring characteristics of a displacement vessel using the RANS code *CFDSHIP-IOWA*, with emphasis on the hull-rudder-propeller interaction.

The numerical model was to be used to evaluate manoeuvring characteristics by numerically performing the tests otherwise included in a physical Planar Motion Mechanism (PMM) test. At Force Technology – Division for Maritime Industry (formerly Danish Maritime Institute) experimental procedures and methods for analysing model scale test results and extrapolation to full scale have been established over a 35-year period. Good general and detailed knowledge of manoeuvring characteristics have consequently been gained during this period. It is recognised, however, that experimental work is both time-consuming and expensive when small alterations to an existing design are made during optimisation of the manoeuvrability of a ship. In addition, PMM testing does not provide detailed knowledge of the flow regimes inducing the measured intergral level forces. Since numerical procedures address both of these concerns Computational Fluid Dynamics (CFD) has been considered as an alternative to experimental work. CFD, has not, however, readily provided a tool for assessing manoeuvring characteristics. To improve on this situation DMI initiated an R&D effort to develop methods in CFD to assess some of the basic hydrodynamic derivatives for a manoeuvring ship.

The motivation for the project was to contribute to an improved understanding of the complex interaction between hull, propeller, and rudder. Better understanding of the flow regime around the stern of the ship, its propeller and the rudder is the key parameter in creating better hull and propeller designs with less cavitation and reduced noise signatures. Furthermore, the procedure developed was to provide a direct analysis of the flow as a basis for manoeuvring models, and the results are expected to contribute to a more accurate and consistent model for the manoeuvrability of ships.

The outcome of the project for all parties involved is to be a numerical procedure capable of analysing the flow around a manoeuvring displacement vessel propelled by conventional propellers in calm water. By application of such a model in the design stage of a new vessel, better understanding of the hydrodynamic characteristics involved in the manoeuvring and propulsion will be obtainable. With an improved understanding of the hydrodynamics during a manoeuvre at hand for the designer of a new vessel, overall improvements on the performance of the final vessel will be obtained. Furthermore, valuable time and money spend on extensive physical model testing required for optimisation may be preserved.

The research effort carries on work in a Ph.D. study performed in co-operation with the Department of Naval Architecture and Offshore Engineering the Technical University of Denmark and Iowa Institute of Hydraulic Research (IIHR) Iowa, USA under the supervision of Fred Stern. This work is documented in Reference /2/.

1.2. Development Objectives

The specific development objectives are described in Reference /1/, and fall into four broad categories:

1. Integration of potential flow propeller computations with RANS appended hull computations, to model circumferentially varying wake fields

2. Enhanced grid generation, using CHIMERA techniques to facilitate the gridding of complex, multiple component grids

3. Numerical studies of propeller-rudder-hull interaction and manoeuvring forces in specific manoeuvring conditions, including verification and validation of the numerical tools

4. Provision of experimental integral and field quantity data for validation

2. Technical Approach: Selection of test cases and conditions

2.1. Test cases

As documented in Reference /3/ *Esso Osaka* was selected as the test hull form, since it is the ITTC standard hull for manoeuvring studies, previous numerical and experimental data existed at Force Technology for this ship and it represents a commercially realistic and challenging hull form for numerical computations.

For the propeller computations on *Esso Osaka* the propeller model was based upon the stock propeller used in the experimental work on this model. This propeller was selected to represent, as nearly as practicable, the propulsion characteristics of the full scale propeller installed on *Esso Osaka*. The model scale was determined from the correct scaling of the model propeller. The ship and propeller characteristics, as modelled, are summarised in Table 2.1.

Esso Osaka **PMM: 278,000 DWT tanker**			
		Ship	**Model**
Scale	-	1 : 1	1 : 43.4783
L_{PP}	m	325.00	7.475
L_{WL}	m	335.00	7.705
B_{mld}	m	53.00	1.219
T_m	m	21.79	0.501
S, incl. rudder	m^2	27671	14.638
∇	m^3	311609.8	3.791
Δ	ton	319400	3.791
C_b	-	0.805	0.805
Number of propeller blades	-	5	4
Propeller Diameter	m	9.100	0.2093
Pitch ratio, $P_{0.7} / D$	-	0.715	0.728
Area ratio, A_e / A_P	-	0.682	0.644
Rudder cord	m	9.00	0.207
Rudder aspect ratio	-	1.54	1.54
Rudder area	m^2	124.65	0.066

Table 2.1 *Esso Osaka* particulars

In support of the development of the propulsion model it was also decided to conduct a limited series of computations on the Series 60 hull, since a grid already existed for this model and good data were available for comparison (see Reference /10/).

For this hull the model length was 4m, and the propeller was a five bladed MAU n=25 as documented in Reference /10/.

2.2. Ship conditions

The tanker *Esso Osaka* was considered at a model scale speed of 0.546 m/s, which, based upon Froude scaling and a model of scale 1:43.4783, corresponds to a full-scale speed of 7 knots and a Froude number of 0.063.

The model Reynolds number was $3.609 \cdot 10^6$, based upon ship length.

For the propelled conditions, the model scale propeller RPM was 236, which was the self-propulsion point derived in the PMM tests.

The ship was computed in a set of defined conditions representing isolated components in the complete equations of motion for a manoeuvring ship, as modelled in a physical PMM experiment. The conditions are 'pure drift' in which the hull maintains a constant speed and angle with respect to the direction of travel, 'static rudder', in which the hull maintains a constant speed and straight-ahead course while the rudder is set to a prescribed angle, and 'pure yaw', in which the hull follows a circular path, with no drift angle. These conditions are defined by the drift angle of the hull relative to the direction of travel (β), the angle of the rudder relative to the hull centreline (δ) and the ratio of the ship length to the circular path radius (r').

The computed conditions for *Esso Osaka* are summarised in Table 2.2. Also noted in that table are the conditions that were used for verification and validation with experimental results.

Type	β (°)	δ (°)	r'
H+R, H+R+P	-4	0	0
H+R, H+R+P	-2	0	0
H, H+R, H+R+P	2	0	0
H^I, $H+R^F$, $H+R+P^I$	4	0	0
H	10	0	0
H	12	0	0
$H+R^F$, H+R+P	0	-10	0
H^I, $H+R^F$, $H+R+P^F$	0	0	0
H+R, H+R+P	0	10	0
H+R	0	0	.1
H+R	0	0	.2
H: Bare hull, H+R: Hull with rudder, H+R+P: Hull with rudder and propeller. ^{I} V&V for integral quantities, ^{F} V&V for field quantities			

Table 2.2 Computed Conditions for *Esso Osaka*

The Series 60 was modelled at a speed of 1m/s, giving a Froude number of 0.16 and a model Reynolds number of $3.96 \cdot 10^6$.

For the propelled conditions the propeller RPM was 468, giving a J of 0.88.

The Series 60 was computed in the bare hull and propelled conditions.

3. Technical Approach: RANS computations

3.1. Numerical Method

The computations were performed with the Reynolds Averaged Navier-Stokes (RANS) solver *CFDSHIP-IOWA*, which, as documented in References /3/, /4/, /5/, /6/, /7/, /8/ and /9/, solves the continuity and unsteady incompressible RANS equations:

$$\frac{\partial U_i}{\partial x_i} = 0$$

$$\frac{\partial U_i}{\partial t} + U_j \frac{\partial U_i}{\partial x_j} = -\frac{\partial \hat{p}}{\partial x_i} + \frac{1}{Re}\frac{\partial^2 U_i}{\partial x_j \partial x_j} - \frac{\partial}{\partial x_j}\overline{u_i u_j} + f_{b_i}$$

where $U_i = (U,V,W)$ are the mean-velocity components, $x_i = (X,Y,Z)$ are the Cartesian coordinates, $\hat{p} = p + Z / Fr^2$ is the piezometric pressure, $\overline{u_i u_j}$ are the Reynolds stresses, and f_{b_i} are the body-force terms, which represent the propeller. The Reynolds stresses are related to the mean rate of strain through an isotropic eddy viscosity v_t :

$$-\overline{u_i u_j} = v_t\left(\frac{\partial U_i}{\partial x_j} + \frac{\partial U_j}{\partial x_i}\right) + \frac{2}{3}\delta_{ij}k$$

where δ_{ij} is Kronecker delta and k is the turbulent kinetic energy. The equations are normalized with ship speed U_0, ship length L_{pp} and water density ρ. Closure of the Reynolds stress problem is achieved by means of the one-equation Baldwin Lomax model for the Series 60 ship and the two-equation k-ω turbulence model for *Esso Osaka*. None of the turbulence models apply wall functions. The code solves the RANS equations on a structured multi block grid by means of finite differencing. For the steady state calculations performed in this context the temporal discretisation is based on a first order backward Euler difference. The spatial discretisation is performed by a second order upwind scheme for the convective terms, while all other first derivatives and viscous terms are discretised by a standard second order central difference scheme. The pressure and the velocities are coupled by means of the PISO method.

The code was run in a fine-grain parallel mode, based on MPI and OPENMP.

For the *Esso Osaka* computations the code utilised the Chimera technique, which is based on substitution of internal regions in the grids with other non-matching grid topologies. The substituted outer grid points (holes) are excluded from the solution by means of value blanking.

In order to apply *CFDSHIP-IOWA* for the current project some modifications of the code were required. The necessary modifications are listed below, and described in Sections 3.3 through 3.7:

1. Modifications to deal with externally generated Chimera grids
2. Calculation of individual surface forces and yaw moments
3. Input of body force data, output of velocity data
4. Scaling of body forces to produce the correct propeller thrust and torque
5. Modifications to deal with the pure drift and pure yaw conditions

3.2. Modelling issues

Conducting numerical computations on geometries of the complexity required in this project at full scale Reynolds numbers would have required a prohibitive number of grid cells. In addition, since model scale experiments were used for verification and validation, computations at full scale would have required scaling between the two sets of results, leading to additional uncertainties with regard to scale effects. For these reasons all computations were conducted at model scale.

Due to the low Froude number wave effects were assumed to be of minor importance, so instead of modelling the free surface a mirror image is applied

3.3. Handling of Chimera grids

In the original version of *CFDSHIP-IOWA* it was possible to work with overlapping grid blocks, but in order to do so it was necessary for the user to put the blocks together manually in a way that secured that the overlap between the blocks was sufficient for the interpolation between the block boundaries. It was not possible to work with interior holes in the grid within a specific block. This meant that it was not possible to handle Chimera grids, in which a region inside a block is replaced by another grid component.

The problem was solved by IIHR personnel, and *CFDSHIP-IOWA* was modified to deal with the new type of grid by using value blanking. The technique involves omitting the blanked point from the CFD solution but keeping track of the points that form the hole boundary to enable data exchange between the outer block and the inserted inner blocks. The features that were added include reading of the file containing the interpolation stencils and the blanking information plus blanking of the hole points.

3.4. Calculation of individual surface forces and yaw moments

Initially *CFDSHIP-IOWA* computed X, Y and Z forces on the total ship grid, i.e. it added the force components from all no-slip surfaces to calculate the total forces acting on the ship. New routines were therefore required to compute loads on different groups of no-slip surfaces in order to isolate force contributions on, for example, the rudder alone or the hull alone.

This modification also required the facility to compute the yaw moment about a defined reference point. At each grid point on the no-slip the contribution to the yaw moment is computed by the cross-product of the vector from the reference point to the grid point with the computed force vector at that point.

3.5. Input of body force data, output of velocity data

Originally *CFDSHIP-IOWA* used internally calculated body forces to model propeller forces, so in order to run the code iteratively with external propeller codes a new set of routines were required.

The first routine reads in the ASCII file containing information about the blocks that contain the propeller, the number propeller points in each block, the grid point locations and finally the body forces.

The second routine searches the grid for propeller points. Prior to writing the velocity output file the routine searches through the grid points to find those within the defined intermediate propeller disk.

The third routine provides the velocity information to be used by the external propeller code. After a complete, converged solution the total velocities from the points in the propeller disk are written out to an ASCII file with similar structure as the body-force file, i.e. containing the number propeller points in each block, the grid point locations and finally the total velocities.

3.6. Scaling of body forces

Included in the body force data file are the total thrust and torque, as computed by the propeller code. After *CFDSHIP-IOWA* has read in the body force data, it is integrated over the propeller disk to compute a total thrust and torque on the propeller disk. In most cases the total thrust and torque computed by the two codes differ slightly, due to the grid differences between the two computations. Prior to the RANS computations, all of the X body forces are therefore scaled by the ratio of the two computed thrust values, and the Y and Z body forces are scaled by the torque ratio.

3.7. Modified far-field boundary conditions

In order to study conditions with steady drift angles and yawing motions it is necessary to impose asymmetrical (with respect to the ship centreplane) far-field boundary conditions. This can be achieved by rotating the ship grid or rotating the inflow velocity. The first method involves no alterations to the *CFDSHIP-IOWA* source code, but requires different grids for each asymmetric case. The second method allows the same grid to be used throughout the computations, with a relatively simple source code change in *CFDSHIP-IOWA*.

The second option was selected, as the easiest to implement and more useful for future work, and the modifications were implemented by IIHR personnel.

The drift condition is modelled by a change of the velocity far-field boundary condition. A feature which allows the user of the code to give the three free-stream velocity components in the input file has been added.

In the pure yaw condition the computation has to be carried out in a rotating coordinate system. Therefore, it has been necessary to include the inertial terms in the momentum equations, which accounts for the Coriolis forces and centrifugal forces. In order to run a pure yaw calculation it is necessary to translate the grid, so that the correct turning circle diameter is obtained. In addition the angular velocity of the system must also be given.

4. Technical Approach: Grid Generation

4.1. Introduction

The goal of the grid generation activities within the project was to make a model of *Esso Osaka* which is based on a grid system that includes the hull form and the rudder represented by their real geometries. The complex geometry of the propeller is not modelled, since the propeller effect is modelled by a body force distribution.

The grid generation and refinement techniques applied are documented in References /3/ and /7/ .

4.2. Applied method

Due to the complexity of the combined rudder-hull geometries it was, from the beginning of the project, realized that it would not be possible to use a single block approach for the grid system, so instead the multi-block approach is applied.

Therefore, the grid is built of patched and overlapping multi block grid components. The overlapping grids are used for inclusion of the rudder, and they are put together by means of the Chimera technique, which joins the grid components by means of automatic hole-cutting. The exchange of data between the boundaries of the hole is performed by tri-linear interpolation and the interpolation stencils required for the data exchange are generated in connection with the hole-cutting. The individual grid-blocks are generated by means of the elliptic and parabolic methods implemented in Gridgen and the Chimera data is generated by the PEGASUS5 code.

The bare hull computations on *Esso Osaka* are performed with an O-O grid consisting of 1,051,440 points. The grid is clustered around the bow and the stern in the main flow direction and close to the hull surface perpendicular to the hull surface. Since the flow is not symmetric both sides of the flow domain around the ship are discretised. On the appended hull the rudder geometry is modelled by an O-H topology with clustering towards the rudder tips in the spanwise direction and near the rudder no-slip surface in the direction perpendicular to the surface. Direct insertion of this relatively fine gridded topology into the relatively coarse hull grids results in orphaned points due to the differences in the grid spacing. Therefore, an intermediate block is introduced for so-called level-2 interpolation. The rudderstock is omitted to simplify the model and reduce the size.

For the propelled model a cylindrical block is located at the propeller position in order to prepare the grid for inclusion of a body-force propeller.

The complete grid system consists of 2,097,006 points distributed on 19 blocks. Since no wall functions are applied, the grid is designed so the near wall spacing of the grid on the no-slip rudder and hull surfaces satisfies $y^+ < 1$. For the fine grid the average of y^+ over the no-slip surfaces is 0.30 for the bare hull and 0.27 for the appended hull.

The complete grid for the rudder, propeller and stern part of the hull is shown in Figure 4.1.

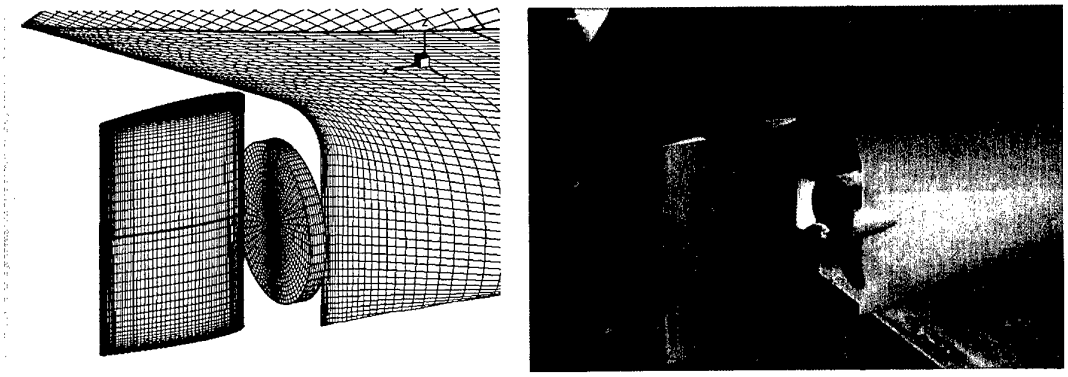

Figure 4.1 a. Hull-rudder-propeller grid. b. Hull-rudder-propeller model.

4.3. Grid Refinement

In order verify the CFD method, solutions obtained on 3 systematically refined grids are required. The grid error contribution is estimated on the basis of generalised Richardson extrapolation, based on the guidelines from ITTC 22nd Quality Manual. The finest grid is the one that is used for data production, while the medium and coarse grids are introduced to estimate the discretisation errors. For many applications grid doubling, i.e. $r_G = 2$, is used, since it is easy to remove every second grid point to arrive at a coarser grid. However, when the grid system models a complex geometry this approach usually does not work. The reason is that it either leads to a fine grid which is too big to be run on the computer or to a coarse grid, which is too coarse to resolve the considered flow problem. Facing this problem, it was decided to use a non-integer refinement ratio $r_G = \sqrt{2}$. Smaller refinement ratios can be used for verification, but the changes between solutions become so small that it is difficult to distinguish the different error and uncertainty contributions.

The generation of the coarser grids involves two tasks. The first task covers generation of the coarse and medium grid topologies based on the fine grid. By removing every second point in the fine grid the coarse grid can be generated, but due to the non-integer refinement ratio the medium grid must be generated by interpolation.

The second task involves the Chimera work, where the grid blocks are put together by hole-cutting and the interpolation stencils for block data exchange are found. However, this is not trivial to do because in order to find valid interpolation stencils the Chimera approach requires a fineness that secures a certain overlap between the blocks. On the coarse grid the overlap is sometimes difficult to maintain and it was found that a working fine grid does not automatically lead to a working coarse grid. The following approach was applied:

1) A fine grid is generated based on previous experience with respect to topology and fineness for hulls and rudders.
2) *PEGASUS* is run to generate the interpolation stencils and the hole definitions.
3) The CFD-code is run to ensure that a converged solution can be obtained with the grid.
4) By removing every second point in the fine grid the coarse grid is generated.
5) *PEGASUS* is run to generate information about holes and interpolation stencils for the coarse grid. If orphaned points occur, it is necessary to go back and improve the fine grid and repeat 4) and 5).
6) After the Chimera data is generated, *CFDSHIP-IOWA* is run to see if a converged solution can be obtained. If the solution diverges, it is necessary to identify the problem and go back and modify the fine grid and repeat the procedure from 4).
7) If convergence is achieved, the medium grid is generated by means of interpolation

8) Information about holes and interpolation stencils for the medium grid is generated by means of *PEGASUS*.
9) *CFDSHIP-IOWA* is run to find the medium grid solution.

Based on the grid generation it was found that when the coarse grid is working it is usually not a problem to get a working medium grid. For the appended hull case, the resulting coarse and medium grids consist of 295886 and 769158 points, respectively, and for the bare hull case they consist of 148149 and 377067 points. The averages of the y^+ values for the coarse and medium grids, corresponding to the case shown for the fine grid in Section 4.2, are 0.64 and 0.44 for the bare hull and 0.54 and 0.38 for the appended hull.

5. Technical Approach: Lifting Line Propeller

5.1. Introduction

As noted in Section 3.1, in *CFDSHIP-IOWA* the propeller is modelled by a distribution of body forces. Initially, the idea in the current project was to make a few test runs with the very simple and prescribed body force propeller model, which was already included in the CFD code. When this was working, the propeller model should be changed to the advanced panel model described above in Section 6. However, the advanced model requires some effort to run, so the idea about a model of intermediate complexity occurred and it was decided to implement a lifting line model. By doing this it is possible to compare the results from the two models and get an idea of how the quality of the propeller results are related to the effort put into running the individual propeller models.

The development of the method was also facilitated by the prior resolution of many of the propeller-RANS interaction issues during the development of the interactive surface panel routines.

As the project progressed, and the lifting line model proved to provide good quality results, emphasis increasingly shifted to the use of this model for the propelled results.

5.2. Propeller model

The use of the lifting line propeller model in the current project is fully documented in References /4/, /6/ and /9/. As documented therein, the lifting line model adopted was outlined in Reference /11/ and used for potential based rudder-propeller-hull calculations, as documented in Reference /12/. The method represents the propeller by a thin disk, in which the finite number of propeller blades is neglected. It is based on a potential theory formulation, in which the propeller is represented by bound vortex sheets on the propeller disk and free vortices shed from them downstream of the propeller. Unlike the prescribed propeller model, this model calculates the body forces based on the effective wake field. This means that the propeller solver is run interactively with the RANS solver. However, in opposition to *ProPulse*, which is an external code, this propeller model is implemented directly in the CFD code.

The axial and tangential body force components are calculated from:

$$fb_x = \frac{A}{\Delta x}\Big[\ \rho V\Gamma(r,\theta)V_\theta(r,\theta) - \frac{1}{4\pi}C_{PD}Nc(r)\sqrt{1+(h/r)^2}V_{0x}(r)V_{0\theta}(r)\ \Big]$$

$$fb_\theta = \frac{A}{\Delta x}\Big[\ \rho V\Gamma(r,\theta)Vx(r,\theta) - \frac{1}{4\pi}C_{PD}Nc(r)\sqrt{1+(h/r)^2}V_{0\theta}^2(r)\ \Big]$$

where ρ, V, C_{PD}, N and $c(r)$ are water density, ship speed, blade section drag coefficient, number of propeller blades and radial cord length distribution, respectively. The constant A is used for bringing the forces into CFD code format:

$$A = \frac{1}{1/2\rho V^2 R_P\,(1-r_h)}$$

$V_x(r,\theta)$ and $V_\theta(r,\theta)$ are the axial and tangential propeller inflow velocities, respectively, $V_{0x}(r)$ and $V_{0\theta}(r)$ are the axial and tangential circumferentially averaged inflow velocities. All 4 velocity components are total velocities interpolated from the RANS solution, so before using them for the propeller solution, the propeller induced velocities are subtracted. Γ is the strength of the vortices on the disk and h is the effective propeller pitch, which is defined by

$$h = \frac{1}{2}\left[a(r) + \frac{r\int_0^{2\pi} V_x(r,\theta)d\theta}{\int_0^{2\pi} (\Omega r + V_\theta(r,\theta))d\theta} \right]$$

where Ω is the angular velocity and $2\pi\, a(r)$ is the effective pitch ratio.

The vortex strength Γ is found from

$$\left[\left\{ \frac{2\sqrt{r^2 + a(r)}}{k_1 r N c(r)} + \frac{r^2 + h^2}{2hr^2 \kappa(r,h)} \right\} V(r,\theta) + (u_p - \frac{h}{r} v_{\theta P}) \right.$$

$$\left. + (V_x(r,\theta) - \Omega a(r) - \frac{a(r)}{r} V_\theta(r,\theta) \right]_{(SP)} = 0$$

which can be solved for $\Gamma(r,\theta)$ when the propeller inflow field and the number of propeller revolutions are known. Finally, $\kappa(r,h)$ represents Prandtl's tip correction factor and k_1 is a correction for the finite width of the propeller blade. Both factors are defined in Reference /12/.

6. Technical Approach: ProPulse propeller code

6.1. Numerical Method

The use of the the surface panel code *ProPulse* is documented in References /3/ and /6/. As documented therein *ProPulse* is an unsteady, potential-based surface panel code, similar to that described in Reference /13/. The surface of the key blade on the propeller is represented by quadrilateral panels. At each time step, the potential at each panel i is given by the solution of the linear system:

$$\sum_{j=1}^{M\cdot N} a_{i,j}\phi_j = \sum_{k=1}^{Z}\sum_{j=1}^{M\cdot N} b_{i,j,k}\sigma_{j,k} - \sum_{k=2}^{Z}\sum_{j=1}^{M\cdot N} a_{i,j,k}\phi_{j,k} - \sum_{k=1}^{Z}\sum_{m=1}^{M}\sum_{l=1}^{Nw} W_{i,m,l,k}\Delta\phi_{m,l,k}$$

where Z is the number of blades, M and N are the spanwise and chordwise number of panels on the blade, respectively, N_w is the chordwise number of panels in the trailing wake, a is the panel-panel dipole influence function, b is the panel-panel source influence function, W is the wake-panel dipole influence function, ϕ is the local potential and σ is the local source strength.

The local source strength σ is dictated by the local onset velocity, which is derived from the input axial, radial and tangential harmonic wake components.

The potential and source strengths are assumed to be constant over each panel, but the panels are not assumed to be flat. The dipole and source potential influence functions are given in Section 6.2.

The wake is assumed to have constant geometry, with $\Delta\phi$ given either by the Kutta condition at the current time step or the circulation at previous time steps, as appropriate.

6.2. Computation of velocities

On the propeller blade the tangential velocities are derived from the numerical differentiation of the panel potentials in the spanwise and chordwise directions. Two approaches were considered for computing the induced velocities at field points outside of the blade: to compute the potentials at a cluster of points close to each field point and then numerically differentiate to find velocities, or to derive new influence coefficients by analytically differentiating the potential influence coefficients. The latter approach was adopted in this project as more robust and efficient.

The potential influence coefficients are computed by two methods, depending on the distance from the singularity panel to the field point. In the far-field point singularities are used, given by:

$$\phi_S = \frac{A}{|\mathbf{R}|}$$

$$\phi_D = \frac{A\cdot z}{|\mathbf{R}|}$$

where ϕ_D is the dipole potential influence, ϕ_s is the source potential influence, A is the panel area, **R** is the vector from the field point to the panel control point and $\boldsymbol{z}$ is the projection of **R** on the panel normal.

In the near field the influence coefficients are the summation of the influences of each panel corner, which are given by:

$$\phi_D = \tan^{-1}\left[\frac{|(\mathbf{R}\times\mathbf{a_1})\times(\mathbf{R}\times\mathbf{a_2})|}{(\mathbf{R}\times\mathbf{a_1})\cdot(\mathbf{R}\times\mathbf{a_2})}\right]$$

$$\phi_S = \frac{-(\mathbf{R}\times\mathbf{a_1})\cdot\mathbf{n}}{|\mathbf{a_1}|}\sinh^{-1}\left[\frac{\mathbf{R}\cdot\mathbf{a_1}}{(\mathbf{R}\times\mathbf{a_1})}\right] + \frac{(\mathbf{R}\times\mathbf{a_2})\cdot\mathbf{n}}{|\mathbf{a_2}|}\sinh^{-1}\left[\frac{\mathbf{R}\cdot\mathbf{a_2}}{(\mathbf{R}\times\mathbf{a_2})}\right]$$

where $\mathbf{R}$ is the vector from the field point to the panel corner, $\mathbf{a_1}$ and $\mathbf{a_2}$ are vectors along the sides of the panel adjoining the corner. After summing the influence of the panel corners an additional term $-(\mathbf{R}\cdot\mathbf{n})\phi_D$ is added to the source potential.

The velocity influence coefficients are given by the analytical differentiation of the above equations in each of the X, Y and Z directions.

6.3. Computation of blade forces

The propeller force is the summation of the unsteady inviscid pressure forces, acting normal to the panel centroids, and the viscous friction forces, acting parallel to the local flow at each panel:

$$\mathbf{F_I} = P\cdot A\cdot\mathbf{n}$$
$$\mathbf{F_V} = C_f\cdot\rho\cdot A\cdot|V|\mathbf{V}$$

where $\mathbf{F_I}$ and $\mathbf{F_V}$ are the inviscid and viscous force vectors, respectively, P and A are the panel pressure and area, $\mathbf{n}$ is the normal vector at the panel control point, C_F is the friction drag coefficient, currently taken to be constant 0.002, and $\mathbf{V}$ is the velocity vector.

7. Technical Approach: Propeller-RANS interaction

7.1. Lifting line

7.1.1. Interaction Procedure

The lifting line propeller model runs interactively with the CFD code, like *ProPulse*. Briefly, the procedure consists of the following steps:

1) A converged solution is calculated for the hull alone.
2) Wake information is extracted from the RANS solution
3) The propeller is turned on to calculate the body-forces based on the wake field
4) The body-forces are then applied to the RANS model, which is run until a converged solution has been obtained
5) A new set of wake data is extracted and corrected for the propeller-induced velocities
6) The procedure is repeated from 3). When the propeller coefficients show convergence the calculation is stopped and the with-propeller solution is found.

7.1.2. Velocity calculation plane

The primary problem related to the iterative coupling between a RANS solver, which works with total velocities, and a potential flow based propeller model, which works with induced velocities, is to find the correct position for extraction of the effective wake velocity field to be used as inflow to the propeller. The total velocity field consists of the hull-induced inflow field and the propeller-induced velocities, so it has to be corrected for the propeller-induced velocities before the propeller model can use it. However, the problem is that the body-forces in the RANS model are applied over a 3D region, whereas the propeller model is based on a cylindrical 2D region, which is located inside the 3D region. When the total velocity field is extracted from the RANS solution it is therefore important to do it at the position that gives an inflow field, which after correction for the propeller-induced velocities is similar to the flow field that the 2D model expects to see. Due to the body-forces in the 3D region, the flow is accelerated through the disk, so in case the 2D propeller plane is located upstream of the correct position, the total velocities are too low leading to a corrected velocity field that is too low, and consequently the propeller loading will be too high. Downstream of the correct position, the opposite happens, i.e. the total velocity is too high, which results in too high inflow velocities to the propeller, which leads to a propeller loading that is too light.

If the fluid velocity is increased ΔU after passing the propeller, the present propeller model is derived to be located at the position where the fluid velocity has increased $\Delta U/2$. In the RANS model the propeller is represented by a disk with thickness Δx and since the velocity increase through the disk is approximately linearly related to the x-position it would be natural to extract the total velocity field in the middle of the disk, i.e. at $\Delta x/2$. However, before initiating all the computations it should be checked if this assumption is reasonable. One way to perform the check is to consider the open-water condition, where the simple uniform propeller inflow field $(U, V, W)=(U_0, 0, 0)$ is known. If the propeller model is turned on in open water and the resulting body-forces are used for a RANS calculation the total velocity field will show a region with increased velocity due to the propeller. Since the propeller is alone this velocity increase is pure propeller-induced velocities. Therefore, if the total velocity is corrected for the propeller-induced velocities the corrected flow field should be close to the uniform inflow field and another iteration with the propeller and RANS models should give approximately the same thrust and torque as for the first iteration. However, this will only be the case if the total velocity field is extracted at the right location.

Therefore, to check the model an open-water solution was calculated on a cylindrical RANS grid and the total velocity field was extracted at $\Delta x/2$.

More details of the influence of velocity calculation plane for the lifting line propeller can be found in Referece /9/.

7.2. ProPulse

7.2.1. Introduction

The use of an external surface panel propeller code, such as *ProPulse*, to generate the body forces introduces a range of additional considerations that must be addressed. These include:

1) Transfer of wake and body force data between the RANS and propeller codes
2) Generation of the correct time-average equivalent body force for input into the RANS code
3) Computation of the appropriate field point locations for computing induced velocities

The particular challenges resolved in this project, which have not been addressed by previous work utilising lifting line and vortex lattice approaches, are outlined herein.

Further details of the interaction algorithms can be found in References /3/ and /4/.

7.2.2. Equivalent body force

As noted in, e.g. Reference /14/, the RANS code requires time averaged, but circumferentially varying, body forces in the propeller disk.

At each instant of time the inviscid blade forces in Section 6.3can be related to local circulation Γ by:

$$\mathbf{F} = \rho \mathbf{U} \times \Gamma dA$$

The correct time average body force at a fixed point in space, however, is not the simple time average of the instantaneous body forces, $\rho \overline{\mathbf{U} \times \Gamma dA}$, but rather the product of the time average circulation and time average velocity $\rho \overline{\mathbf{U}} \times \overline{\Gamma dA}$. This calculation requires the calculation of the velocities and circulations at each control point, for each time step in the propeller calculation. In a vortex lattice approach, as used for example in Reference /14/ the propeller blade is infinitely thin, so the inflow velocity is constant on the two sides of the blade, and the circulation at each panel is taken to be $2\rho\Delta V$. In the surface panel method, however, the inflow velocity and panel area at two panels on opposite sides of the blade cannot be considered constant, so the equivalent circulation was taken from the force identity:

$$\rho\Gamma = \frac{P \cdot \mathbf{n} \times \mathbf{V}}{|\mathbf{V}|^2}$$

7.2.3. Field point locations

In the lifting line approach outlined in Section 5, the propeller is assumed to lie on a constant-X plane, which is consistent with the RANS grid geometry. Thus all velocities can be computed at a single plane. For body-fitted grids, such as applied in vortex lattice and surface panel codes, however, the field points

must conform to the propeller geometry, to ensure that the field points are at consistent locations relative to the local blade geometry. In addition, the computation of equivalent body forces requires the time average velocity at each blade control point, for each time step.

To avoid the singular behaviour near panel edges, vortex lattice approaches typically define field points fixed in space, coinciding with the positions of the control points on the key blade at time step 0, and then at equal angular increments around the circumference of the propeller disk. The angular increments are specified to coincide with the propeller stepping in the unsteady propeller solution, thus ensuring that, at each time step, each field point is either exactly at a blade control point or at some integral multiple of an incremental angular distance from it.

In a surface panel program, such an approach cannot be adopted, since at some time steps field points will lie interior to the propeller blade, and at other time steps they will lie at inconsistent distances from the high pressure and low pressure sides of the blade. Because of the steep velocity gradients near the blade surface, this leads to erroneous computations of average velocity.

In this project, therefore, the solution adopted was to locate the field points on a rotating grid between the key blade and the following blade. Field points were placed in a series of circumferential arcs, starting at a control point on one side of the key blade and ending at the corresponding control point on the opposite side of the next blade. This also simplifies the velocity computation in the propeller code, since the field points remain fixed with respect to the rotating propeller grid.

To compute propeller-induced velocities in the hull-fixed coordinate system, for each time step in the unsteady propeller solution, the velocities on the rotating field point grid are interpolated onto a fixed polar grid with even angular increments, for one 360° sweep of the key blade. These interpolated velocities are then time averaged to derive the time average velocities at each position on the fixed grid. The time averaging procedure yields the time-averaged forces on the intermediate propeller grid, i.e., on a regular cylindrical grid, with radial distribution dictated by the ProPulse spanwise panel distribution and even angular increments. The body forces per unit volume are then given by dividing each time-averaged force by the volume of the angular sector, $\frac{1}{2}(r_{n+1}^2-r_n^2)\, d\theta dx$, and nondimensionalised for *CFDSHIP-IOWA* by the factor $LPP/(\rho V_A^2)$.

As noted in Section 7.1, the other fundamental constraint on the field point locations is the requirement to obtain propeller-induced velocities at the correct point for subtraction from the RANS computed velocities. In the lifting line approach the induced velocities follow a step function, so it is relatively easy to correlate them spatially with the velocity increase through the RANS propeller disk. For 3D codes, such as vortex lattice and surface panel codes the velocities are primarily induced by the trailing wake, so the spatial evolution of the velocities is not necessarily correlated with the RANs velocities, depending on the sptail extent of the RANS propeller disk.

In Reference /10/ the vortex lattice induced velocities were pragmatically taken at the mid-chord point, and thickness effects ignored. In a surface panel method, such as *ProPulse*, the thickness effects are an intrinsic part of the solution for surface potentials, and cannot be ignored, so the mid-shord positions are not the correct ones for the induced velocities. In this project a position just aft of the blade leading edge was adopted as the optimum location for computing induced velocities, and the RANS total velocities were taken to be those at the forward face of the cylindrical propeller grid. These positions were found to provide the best correlation between RANS and potential flow induced velocities.

These effects are illustrated in Figure 7.1, which shows the spatial evolution of the axial and tangential velocities computed for the Series 60 propeller in open water at r/R of approximately 0.7.

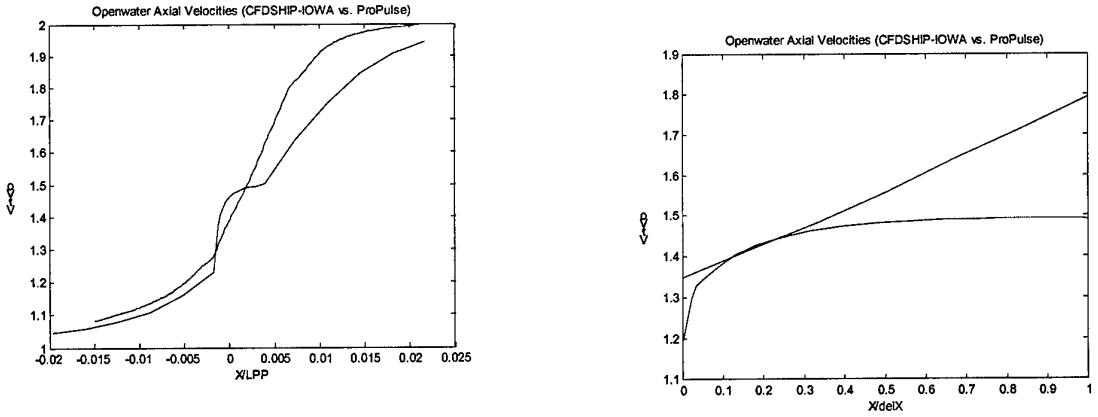

Figure 7.1 Evolution of axial and tangential induced velocities for Series 60 propeller

8. Technical Approach: PMM Tests

8.1. Introduction

To provide validation data for the integral force and moment quantities tests were conducted on the large-amplitude PMM at DMI, on a 1:43.4783 scale model of the *Esso Osaka*. This model had been previously tested as part of the PhD project documented in Reference /2/. For the purposes of this project slight modifications to the model, and additional conditions and force measurements, were required.

8.2. Model modifications

For the PMM tests in the PhD project the model included a rudder heel and fairing around the rudder stock, to simulate the full-scale *Esso Osaka* geometry. These features have been omitted from the CFD grid, however, to reduce the grid complexity. Since the purpose of the PMM tests in the current project was to validate the CFD calculations, rather than predict the full-scale manoeuvring characteristics, these features were also removed from the physical model. Since the lines of the skeg had been slightly modified to fair in the rudder heel, removal of this feature necessitated cutting away a small piece of the skeg, between its trailing edge and station 0.75, and replacing it with a foam piece. This piece was faired to give a continuous thickness, vertical skeg trailing edge.

As part of the uncertainty analysis procedure templates were constructed for Stations -0.25, 0.0, 0.25, 0.50, 0.75, 1.0, 1.25, 1.50, 1.75, 2.0, 2.5, 3.0, 4.0 and 5.0. These templates were checked against the port side of the hull, on the previously marked station lines.

In PMM tests at DMI the rudder stock is normally mounted in a force gauge assembly which sets the rudder angle using an electric motor and rotates with the rudder stock, to measure the rudder forces in rudder coordinates. In the current project it was desired to measure rudder forces in the ship coordinate system, to remove the angular error in the force transformation as a potential error source. In addition, it was desired to set the rudder angle more precisely than is possible with the standard system, which sets the rudder angle to a series of set points. For these reasons a special rudder mounting arrangement was devised, with the rudder stock passing through a through-hull fitting and cantilevered from a force block held fixed in the hull. The rudder angle was set using the same drive circuit, but with a continuously variable potentiometer to set the angle, rather than discrete switches. A tiller was mounted on the top of the rudder stock, which allowed visual checking of the rudder angle relative to a large quadrant mounted to the ship.

The propeller, motor, turbulence stimulation, and ballasting were all as in the previous tests on the model.

8.3. Test conditions

Ordinarily at DMI PMM tests are conducted to derive the manoeuvring characteristics of ships in full four-quadrant manoeuvring scenarios. In this project, since the purpose of the tests was to validate CFD computations at selected operating conditions, only a small subset of the full four-quadrant test matrix were used.

The test conditions are outlined in Tables 8.1 and 8.2.

Drift angle	Rudder angle	Motor RPM	Yaw rate (r')
Search for self-propulsion point:			
0	0	190, 210, 230, 250, 270	0
Rudder angle variation, self-propulsion point:			
0	0, 5, 10, -5, -10	236	0
4	-5, -10	236	0
-4	5, 10	236	0
Rudder angle variation, high RPM:			
0	0, 10, –10	295	0
Drift angle variation, self-propulsion point:			
0, -2, -4*, -10, 2, 4, 10	0	236	0
Yaw rate variation, self-propulsion point:			
0	0	236	0.1, 0.2, 0.5

Table 8.1 PMM validation test conditions: with propeller

Drift angle	Rudder angle	Motor RPM	Yaw rate (r')
Rudder angle variation, no propeller:			
0	0, 5, 10, -5, -10	-	0
-4	5, 10	-	0
4	-5, 10	-	0
Drift angle variation, no propeller:			
-2, -4, 2, 4	0	-	0
Yaw rate variation, no propeller:			
0	0	-	0.1, 0.2, 0.5
Drift angle variation, no rudder or propeller:			
0, -4, -8, -10, -12, -16, -20, 4, 8, 10, 12, 16, 20	-	-	0

Table 8.2 PMM validation test conditions: no propeller

In all cases the model speed was set to 0.546 m/s, to model a 7 knot approach speed, as in the CFD work. The test conditions above were designed to replicate the conditions studied in the CFD work.

8.4. Test procedure

Insofar as possible the tests were carried out in accordance with DMI standard practice, to provide a quality check on those procedures. The model was ballasted, swung, attached to the PMM mechanism and aligned in the towing tank, and the instrumentation was calibrated, according to established DMI procedures. In addition, for those conditions at which uncertainty analyses are not carried out, the tests were conducted according to established procedures.

For the uncertainty analyses a modified procedure was adopted. Each of these tests was conducted a total of 15 times, in 3 sets of 5. In the first set of tests the entire test programme above was conducted, with one test in each condition. The tests for uncertainty were then carried out a further four times each. The model was then dismounted from the PMM mechanism and the PMM strongback from the carriage, and the carriage used for a short time on another project. The model was then re-mounted to the PMM,

and the tests for uncertainty repeated 5 more times each. During these repeat tests, the conditions were varied for each run, to avoid repeat runs in the same condition. The model and PMM were then, again, dismounted and remounted. A third set of 5 repeat tests was then conducted. This procedure was adopted as a compromise between completely re-rigging the model between each set of repeats and leaving the model attached to the PMM mechanism throughout.

8.5. Data analysis

The static drift and rudder angle tests were analysed by simply taking the mean of the measured forces through each run. A low-frequency oscillation was noted in the hull X and Y force data in some of the drift angle tests, so analysis software was developed which allowed the interactive windowing of the measurement time traces, which enabled windowing of the time traces to contain integer numbers of oscillations.

The dynamic runs were analysed with proprietary PMM analysis software at DMI, which fairs through rapid force oscillations during each run to find the underlying low-frequency forces oscillating at the PMM frequency. These faired forces are then found at the four cardinal points, at which the yaw rate and acceleration are at extrema.

From these data curve fits are used to find the coefficients for the polynomial approximations for the force coefficients, which take the form:

$$C'(\cdot 10^5) = C'_0 + C'_{r'}\, r' + C'_{\dot{r}'}\, \dot{r}' + C'_{r'r'}\, r'^2 + C'_{r'r'r'}\, r'^3$$

where r' is the non-dimensional maximum yaw rate, $\psi' LPP/U$, achieved when the model is at the outer extrema of the oscillations.

The software has the facility to analyse single runs, all runs at a single yaw rate, runs at all rates, etc.

The uncertainty in the PMM results was assessed according to a modified version of the procedures recommended by the ITTC.

The precision limits for the repeat runs were taken to be

$$P_r = \frac{KS}{\sqrt{M}}$$

where the coverage factor K was taken to be 2 for 95% confidence limits.

The contributory sources of bias errors were taken to be:

1. Model geometric error
2. Ballasting error
3. Force calibration non-linearity
4. Model alignment

If it is assumed that forces are proportional to wetted surface, particularly at the low Froude numbers in these tests, then the bias errors associated with geometric errors are given by

$$B_{WS} = \frac{\Delta WS}{WS} \cdot \bar{F}$$

where WS is the model wetted surface, ΔWS is the wetted surface error associated with manufacturing and ballasting errors, and F is the mean force in a given run.

The ITTC recommend the following form for estimating the bias limit associated with a linear fit to a scattered set of calibration measurements:

$$B = K \cdot \sqrt{\frac{\sum (Y_i - (aX_i + b))^2}{M-2}}$$

with a coverage factor K equal to 2 for 95% confidence limits. This approach is appropriate to a large number of randomly scattered calibration errors, but not to a relatively small number of systematic non-linearities. The most appropriate method for dealing with non-linearities in force calibrations is to adjust each measured point in each time series for the calibration error. In this analysis a compromise technique was utilised, in which the errors were assumed to be approximately constant throughout the measurement range, and thus each measured point is subject to this constant error. In this case the calibration bias error is given by:

$$B_{C1} = \sqrt{\frac{\sum (Y_i - (aX_i + b))^2}{M}}$$

At several points throughout the tests the force calibrations were checked in-situ. The bias errors associated with these checks are given by:

$$B_{C2} = \frac{\left|\frac{\sum \Delta F_i}{M}\right| + \frac{K \cdot S}{\sqrt{M}}}{|F_N|} \cdot \bar{F}$$

where ΔF_i are the errors of the individual calibration measurements, K is the coverage factor (again, taken to be 2), S is the standard deviation of the calibration measurement errors and F_N is the nominal calibration force applied.

Finally, the force errors associated with alignment errors are given by:

$$B_\beta = \tan^{-1}\left(\frac{\Delta Y}{L_F}\right)\frac{\partial \bar{F}}{\partial \beta}$$

where ΔY is the transverse error of the stem, relative to the tank centreline, L_F is the length from the PMM pivot to the stem measurement point, and $\frac{\partial \bar{F}}{\partial \beta}$ is the average slope of the force with respect to drift angle.

The total uncertainty is given by:

$$U_T = \sqrt{P_r^2 + B_{Ws}^2 + B_{C1}^2 + B_{C2}^2 + B_\beta^2}$$

9. Technical Approach: PIV velocity measurements

9.1. Introduction

To obtain validation data on velocities near the stern of the model it was decided to utilise the particle image velocimetry (PIV) technique in the DMI towing tank, using the same model as used in the PMM tests. The decision to conduct the tests in the DMI towing tank, with the PMM model, was taken to assure exact geometric and flow similitude between the two sets of tests. The PIV technique was selected for several reasons. Firstly, it is a non-intrusive technology, i.e. there are no pressure or optical probes in close proximity to the measurement volume. Secondly it is likely to be more accurate than pressure measurements at the low velocities and high cross-flow angles at the stern of this model (though less accurate than LDV). Thirdly it is a more efficient technique for acquiring velocity data in large volumes than point measurement techniques such as LDV and pressure measurements. Since DMI has no equipment or prior experience with this technique SIREHNA in Nantes, France were sub-contracted to provide equipment and expertise for these tests.

9.2. PIV Equipment

The SIREHNA PIV system is a 2D system, consisting of an underwater optical head for generation of the laser sheet and two underwater cameras, held on a common L-shaped mast to maintain a fixed distance between the cameras and the laser sheet. Two cameras are utilised to double the data acquisition rate.

The optical head contains a scanning mirror linked by fibre optic cable to a 2W laser source.

The field of view of each camera is approximately 300mm x 400mm. After digitising the image resolution is 640 x 480 pixels. The camera fields of view were overlapped by approximately 20mm, since velocity vectors cannot be found at the image edges.

Each camera is linked to a separate PC equipped with a frame grabber. The PCs are linked by a local Ethernet to synchronise the data acquisition.

The cameras operate at a frame rate of 60 hz, which is also used for the laser scanning frequency. The hard disk storage allows a maximum of 1200 images per camera. The equipment normally works at a constant frame rate, which would provide a 20 second run length. It was decided that this was too short a run length, so the acquisition software was modified to capture alternate pairs of images, thus doubling the run length and reducing the effective sampling rate to 15 hz.

For vertical planes the cameras were fixed to the vertical leg of the L-shaped mast, and the laser optical head to the bottom leg, and for horizontal planes the positions were reversed (see Section 9.6).

9.3. Seeding equipment

To ensure adequate underwater seeding a special seeding rake was constructed by SIREHNA, consisting of a horizontal feed pipe at the top connected to a row of vertical pipes with small drilled holes for dispensing an even cloud of seeding throughout the measurement volume.

The rack was mounted on vertical pipes, which permitted raising and lowering between seeding runs.

In some tests it was also found necessary to seed from an aerial spray diffuser, to replenish the seeding near the free surface, due to the sinkage of seeding particles during the seeding operation.

9.4. Carriage mounting and traversing equipment

The model was fixed to the aft end of the towing tank carriage by means of vertical wooden struts fore and aft, and a steel pole amidships. The system was designed to allow the fitting of the traversing rig and PIV equipment on the model freeboard aft of the carriage, accessible by platforms, whilst maintaining a fixed position relative to the free surface. Yaw angle was adjusted by pivoting about the steel pole, and yaw angle, trim, heave and roll were held fixed by screws in the wooden struts.

The traversing system to hold the PIV mast was constructed primarily of aluminium box girders. A sub frame was fixed to the model freeboard. A secondary frame was mounted on linear tracks, allowing fore-and-aft movement, and a sliding transverse arm was mounted on linear tracks on the secondary frame. At the end of the transverse arm was a vertical strut with vertical linear tracks, on which the PIV mast was mounted.
The system thus allowed PIV system movement in the X, Y, and Z directions. Positions were fixed by pins passing through brackets on the moving parts and held in locator holes in the fixed parts. Each set of locator holes were predrilled at a sequence of predetermined relative positions on a graduated scale. After mounting the PIV equipment on the mast, the positions of the scales were set on the traverse frames by using the laser sheet reflection on the hull surface as a guide line. The weight of the vertical mast was taken by an overhead block and tackle, to reduce the heeling moment on the model and the stress on the vertical locator pins. No mechanical traversing system was employed, as manual location of the traversing rig was easily done within the return seeding run between each measurement run (see Section 9.8).

The horizontal and vertical orientations of the model, traversing rig and PIV mast were checked by digital level.

Fixing the traversing rig relative to the model, rather than the carriage, removed the positional errors associated with relative movement of the model.

Figure 9.1 shows the PIV mast, traversing rig and carriage fixing system as installed.

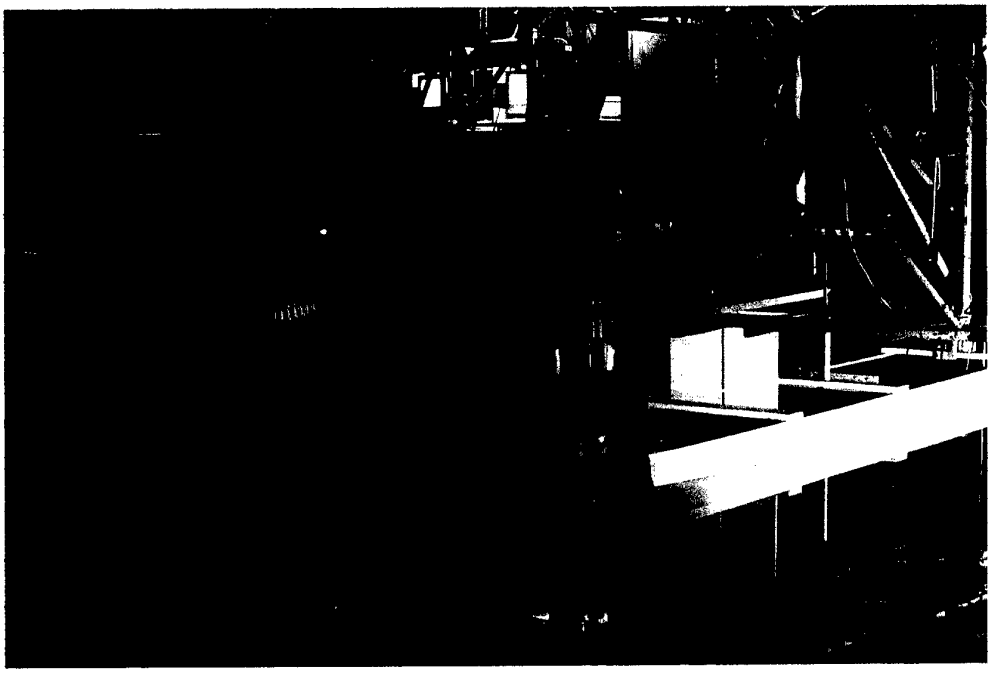

Figure 9.1 PIV system installed

9.5. Operating conditions

For these tests it was decided to focus on four key operating conditions:

1. 0° drift, 0° rudder, no propeller
2. 0° drift, 10° rudder, no propeller
3. 4° drift, 0° rudder, no propeller
4. 0° drift, 0° rudder, propeller at self-propulsion point

These tests provide a good range of data on the most important interactions to model in the CFD calculations, i.e. hull with drift, hull-rudder, hull-propeller-rudder.

The tests were split into two test sessions: the first with no drift and no propeller, (conditions 1 and 2 above) and the second with drift or propeller (conditions 3 and 4 above).

The first set of tests were conducted in July-August, 2001, and the second set in October-November, 2001.

9.6. Measurement planes

To study the development of flow patterns at the stern of the model 3D velocity measurements were required on transverse planes at Stations 0.5, 0.16 (propeller plane), 0.0 and -0.25. Since the SIREHNA PIV system is a 2D system, two sets of planes are required to capture 3D velocities. Initially it was anticipated that the system could measure the V and W components directly in the transverse planes, and the U and W velocities in longitudinal planes parallel to the centreplane of the model.

During initial tests on the system in open water, it was found that measurements in the transverse planes were not possible with the desired accuracy. Therefore, it was decided to alter the system, so that U, V velocities were measured in horizontal planes, and U, W velocities in longitudinal planes. The horizontal and longitudinal planes used in the test are listed in Table 9.1 and shown in Figure 9.2.

Horizontal planes (mm below surface)	**Vertical planes (mm from centreline)**
70	0
100	15
130	29.9
160	44.9
190	59.8
220	89.7
250	119.6
280	164.5
310	239.2
340	314.0
370	388.7
400	
430	
460	
485	
520	
550	

Table 9.1 PIV measurement planes

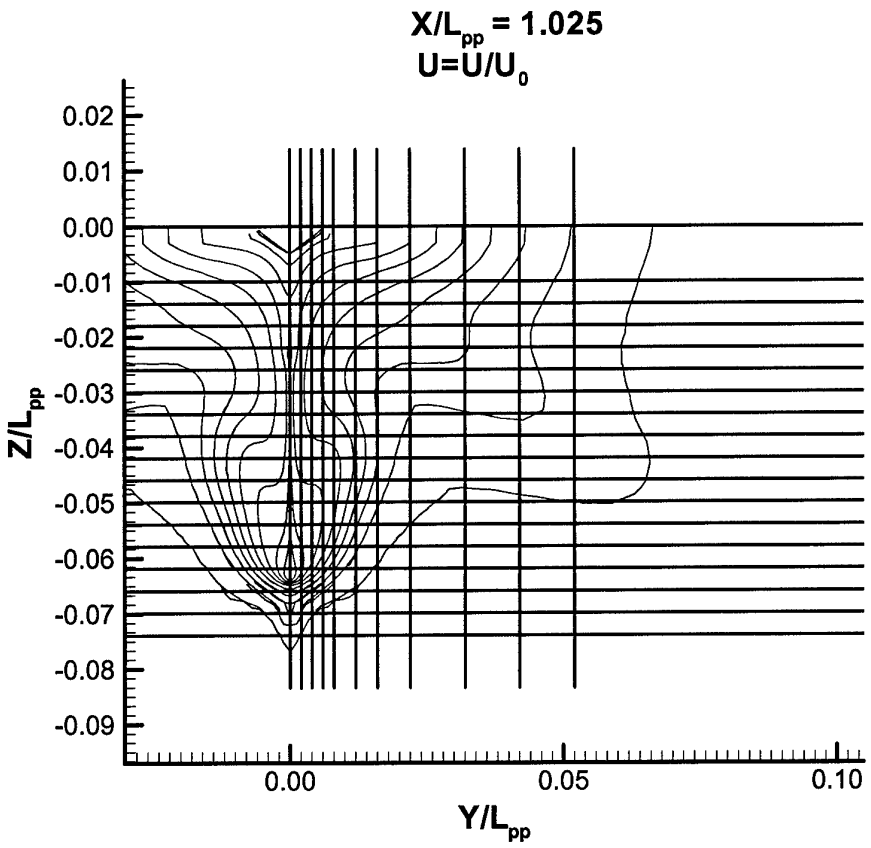

Figure 9.2 PIV measurement planes

Both sets of planes were set in X to cover the full range of transverse planes listed above.

For cases 1, 2 and 3 measurements were taken on the starboard side of the hull, with positive and negative angles applied to provide data for the two sides of the hull. For case 4 the traversing rig was moved to the port side to measure the port side data.

9.7. Calibration procedure

Prior to the tests a gridded calibration plate was held at the plane of the laser sheet, perpendicular to the camera line of sight. The precise spacing of the grid lines on this board provided calibration data to convert camera pixels to physical distance in the laser plane. This procedure was repeated for the vertical and horizontal planes.

For vertical planes the verticality of the laser sheet was checked by shining the sheet along a plumb line suspended from the model, and by visually sighting the reflection of the sheet along the transom of the model. The level of the horizontal planes was checked by aligning the laser sheet parallel to the free surface.

The position of the laser sheet was fixed with respect to the model by capturing images of the model with plumb lines hanging from specific points on the model, e.g. along the transom centreline and from the sides of the traversing rig frame. Additionally, the positions of the rudder trailing edge top and bottom within the captured images were used to maintain consistent positioning between series of runs.

9.8. Test procedure

Prior to each test run, while the water settled from the previous run, the tank of seeding fluid was filled with a mixture of water and seeding particles, to be ready for seeding at the end of the run. The model was then run up to speed and image capturing commenced when the laser sheet was visibly in the densely seeded area of the tank. Image pairs were captured, at a rate of 1/60 s between images within a pair and 1/15 s between pairs, for 40 seconds, giving 600 pairs of images per run. When real-time observations of the captured images indicated holes in the seeding during the run, multiple runs were used at a single measurement plane to give a total of 600 good image pairs.

At the end of each run the seeding rake was lowered into the water, and seeding fluid ejected during the slow (0.1 m/s) backwards run to the start point. During this time the traversing system was moved to the desired position for the next run.

9.9. Data analysis

SIREHNA were largely responsible for analysing the captured images to derive velocities, including checking for seeding quality and deriving the necessary transformations from the calibrations, etc.

The image analysis is performed using the *VIDPIV 4.0g* software, distributed by Intelligent Laser Applications.

The analysis is composed of two main steps: global cross-correlation and adaptive cross-correlation, each of which consists of global filtering, local filtering, interpolation and smoothing procedures. Different window sizes and movement step sizes were tested, to find the set of parameters that provided the best valid vector rates. The final parameters are a window size of 32 pixels x 32 pixels (equal to 22mm x 22mm), moved by 32 pixels for the global cross-correlation and moved 16 pixels for the adaptive cross-correlation. The velocity maps are provided with a regular mesh of 16 pixels in both directions.

For each camera, for each run, are provided the mean and RMS U, U and W velocities, together with the mean values of U·U, U·V, V·V, or U·U, U·W, W·W.

10. Technical Approach: Verification and validation at integral level

10.1.1. Introduction

Since the RANS technology is applied to the relatively new area of manoeuvring, and due to the complexity of the flow problem, it is required to investigate the performance of the computational method. The approach is first to estimate the numerical uncertainties through verification and second to quantify the difference between the numerical results and experimental data through validation.

The verification and validation exercises for the integral level quantities are documented in References /3/ /4/ /7/, and summarised herein.

10.2. Verification and validation methodology

Depending on whether the numerical error is treated as stochastic or deterministic, there are two approaches to be followed: uncorrected or corrected. Common to both of these is that they are based on the simulation error δ_S, which is defined as the difference between a simulated result S and the true value T. The simulation error is composed of two contributions, the numerical errors δ_{SN} and the modelling errors δ_{SM}, i.e. $\delta_S = S - T = \delta_{SN} + \delta_{SM}$. In some cases the conditions allow the sign of the error to be estimated by $\delta_{SN} = \delta^*_{SN} + \varepsilon_{SN}$, where δ^*_{SN} is the estimate of the error and its sign and ε_{SN} is the error of the estimate. In this case the corrected approach can be followed, i.e. the error estimate is used to correct the numerical solution in order to obtain the numerical benchmark S_C defined by:

$$S_C = S - \delta^*_{SN}$$

Verification is defined as a process for assessing simulation numerical uncertainty U_{SN} if the uncorrected approach is followed and for estimating the sign and magnitude δ^*_{SN} of the numerical error, together with the uncertainty of the error estimate U_{S_CN}, if the corrected approach is followed. For the uncorrected case, the error is assumed to consist of contributions from the number of iterations δ_I, the discretisation of the grid δ_G and other parameters δ_P. This leads to the following expression for the simulation numerical uncertainty:

$$U^2_{SN} = U^2_I + U^2_G + U^2_P$$

When the error is estimated following the corrected approach, the solution is corrected in order to obtain the numerical benchmark S_C. In this case the estimate of the simulation numerical error δ^*_{SN} and the corrected uncertainty U_{S_CN} are given by:

$$\delta_{SN} = \delta^*_I + \delta^*_G + \delta^*_P$$

$$U^2_{S_CN} = U^2_{I_C} + U^2_{G_C} + U^2_{P_C}$$

Validation is defined as a process for assessing simulation model uncertainty U_{SM} by using benchmark experimental data D, and when conditions allow it, estimating the sign and magnitude of the modelling error δ_{SM} itself. One of the key parameters in the validation is the comparison error E, which is defined as the difference between the data D and the simulation S values:

$$E = D - S = \delta_D - (\delta_{SN} + \delta_{SM})$$

The modelling errors δ_{SM} can be divided into modelling assumptions, such as boundary conditions, turbulence models etc., and the use of prescribed data such as fluid properties. Another quantity, which is used to determine if validation has been achieved, is the validation uncertainty U_V defined by:

$$U_V^2 = U_D^2 + U_{SN}^2$$

When the comparison error E and the validation uncertainty U_V are determined they are compared. If $|E| < U_V$, the combination of all the errors in D and S is smaller than U_V and validation is achieved at the U_V level. If $U_V << |E|$ the numerical simulation and the data errors δ_{SN} and δ_D are small compared to the numerical modeling error δ_{SM} leading to $E \approx \delta_{SM}$. Therefore, the sign and magnitude of E can be used to make model improvements.

For the corrected approach the expressions for E and U_V are

$$E = D - S_C = \delta_D - (\delta_{SM} + \varepsilon_{SN})$$

$$U_{V_C}^2 = U_{E_C}^2 + U_{SM}^2 = U_D^2 + U_{S_C N}^2$$

10.3. Verification procedure

Focus is placed on the uncertainties and errors from the dicretisation, i.e. the grid and the iterative solution procedure. The iterative uncertainty U_I is estimated on the basis of the convergence history of the forces and moments from the fine grid solution by

$$U_I = \left| \frac{1}{2}(S_{1U} - S_{1L}) \right|$$

where it is attempted to bound the error based on S_U and S_L, which are the upper and lower envelopes of the solution.

The grid errors and uncertainties are estimated based on convergence studies of multiple grid solutions obtained with three systematically refined grids. By means of the change between coarse and medium grid solutions $\varepsilon_{G_{32}} = S_3 - S_2$ and the change between medium and fine solutions $\varepsilon_{G_{21}} = S_2 - S_1$ it is possible to calculate the convergence ratio R_G defined by

$$R_G = \frac{\varepsilon_{G_{21}}}{\varepsilon_{G_{32}}}$$

The convergence ratio is used to determine the type of condition. There are three possible conditions:

(*i*) Converging condition: $0 < R_G < 1$
(*ii*) Oscillatory condition: $R_G < 0$
(*iii*) Diverging condition: $1 < R_G$

In case condition (*i*) occurs, grid convergence is achieved and it is possible to use generalized Richardson extrapolation (RE) to estimate U_G or U_{GC} and δ_G^*, as described below. For the oscillating condition (*ii*) the uncertainty is estimated by bounding the error based on the maximum S_U and the minimum S_L of the oscillation, i.e.

$$U_G = \frac{1}{2}(S_U - S_L)$$

For the last condition (*iii*) it is not possible to estimate the errors and uncertainties.

As mentioned above, the converging condition (*i*) allows the generalized RE to be used for estimation of the grid error δ_G^*, but also of the order of accuracy p_G. The estimate is based on an expansion of the error in a power series with integer powers of the grid refinement ratio $r_G = \Delta x_{G2} / \Delta x_{G1} = \Delta x_{G3} / \Delta x_{G2}$ as a finite sum. Since only three grids are considered in this context, only the leading term in the series can be estimated. This results in the following one-term estimates for the error and order of accuracy:

$$\delta_{RE_{G1}}^{*(1)} = \frac{\varepsilon_{G_{21}}}{r_G^{p_G} - 1}$$

$$p_G = \frac{\ln\left(\frac{\varepsilon_{G_{32}}}{\varepsilon_{G_{21}}}\right)}{\ln(r_G)}$$

When doing verification for complex grids it is difficult to determine if the solutions are in the asymptotic range, which is essential for an accurate estimation of the order of accuracy and consequently of the error. Therefore correction factors, based on verification of analytical benchmarks, are introduced. The correction factor is used as a quantitative metric for the proximity of the solutions to the asymptotic range and for improving the estimates of the errors and uncertainties. When the correction factor C_G is introduced the expression for the error becomes:

$$\delta_{G1}^* = C_G \delta_{RE_{G1}}^* = C_G \left(\frac{\varepsilon_{G_{21}}}{r_G^{p_G} - 1} \right)$$

where

$$C_G = \frac{r_G^{p_G} - 1}{r_G^{p_{Gest}} - 1}$$

Depending on whether the correction factor C_G is close to 1 or not, two cases are to be considered when the numerical uncertainties are estimated. If C_G is sufficiently larger or smaller than one, i.e. the solution is far from the asymptotic range, the grid uncertainty is estimated by:

$$U_G = \left[2\left|1 - C_G\right| + 1\right]\left|\delta^*_{RE_{G1}}\right|$$

The other case occurs if the solution is close to the asymptotic range, i.e. C_G is close to 1. In this case the uncertainty U_{GC} is calculated from

$$U_{GC} = \left|1 - C_G\right|\left|\delta^*_{RE_{G1}}\right|$$

11. Technical Approach: Verification at field quantity level

11.1. Introduction

Verifying and validating the CFD code at the integral level demonstrates how the code performs globally. In order to get information about the capability of capturing the details of the flow field itself it is necessary to work with the field quantities. The idea in the present project is to consider the three velocity components (U, V, W) along constant waterlines in the stern region of the ship, go through the verification and validation procedures described above and thereby obtain information about the code performance in connection with flow field predictions.

11.2. Verification procedure

The theory presented in Section 10 is valid for both integral and field quantities, but there are problems related to evaluation of the convergence ratio R_G, the order of accuracy p_G and the correction factor C_G. The reason is that the ratio between the solution changes $\varepsilon_{G_{21}}$ and $\varepsilon_{G_{32}}$ becomes ill-defined in cases where both of the changes go to zero. In order to overcome this problem, two approaches can be used, depending upon the observed type of convergence in the considered collection of points. The first approach is based on group-averaged values $\langle R_G \rangle$ and $\langle p_G \rangle$ for the convergence ratio and the estimated order of accuracy, respectively. The two quantities are defined as

$$\langle R_G \rangle = \left\| \varepsilon_{G_{21}} \right\|_2 / \left\| \varepsilon_{G_{32}} \right\|_2$$

$$\langle p_G \rangle = \frac{\ln\left(\left\| \varepsilon_{G_{21}} \right\|_2 / \left\| \varepsilon_{G_{32}} \right\|_2 \right)}{\ln(r_G)}$$

where $\langle\ \rangle$ and $\|\ \|_2$ denote averaged quantities and L2 norms of the solution changes in the considered collection of points, respectively.

The verification of the uncorrected solution is carried out by means of the equations in Section 10, which give U_G in the considered points, based on $\varepsilon_{G_{21}}$ and $\langle p_G \rangle$. For the corrected solution the procedure is similar, so $\langle p_G \rangle$ is used to estimate δ^*_{G1} and U_{Gc} at the field points. After estimating the point uncertainties an L2 norm of the error and uncertainty distributions is used to assess the global level of verification.

The second approach is more appropriate to use if a dominant part of the point variables show oscillatory convergence. In this case all the uncertainties are estimated as if all points showed oscillatory behaviour. This means that the point uncertainty U_G is found as the absolute value of half of the difference between the maximum and minimum values obtained from the solutions on the three grids, i.e.:

$$U_G = \left| \frac{\max(S1, S2, S3) - \min(S1, S2, S3)}{2} \right|$$

After estimating all of the U_G values an L2 norm of the uncertainty distribution is again used to assess the global level of verification.

12. Results: Verification and validation

12.1. Integral level quantities

The verification and and validation of the hydrodynamic force computations for the bare *Esso Osaka* hull and appended hull documented in References /3/ /4/ /5/ and /7/. Reference /7/, in particular, documents the iteration and grid uncertainties.

A brief summary of these results is contained herein, and reference should be made to the above documents for further details.

The forces and moments are non-dimensionalised by the water density ρ, ship speed U, ship length L_{pp} and draft T by means of the following expressions:

$$X' = \frac{F_X}{0.5\rho U^2 L_{pp} T}, \quad Y' = \frac{F_Y}{0.5\rho U^2 L_{pp} T},$$

$$N' = \frac{M_Z}{0.5\rho U^2 L_{pp}^2 T}$$

Table 12.1 presents the results for the bare hull sailing straight-ahead. For this condition the method is verified at a level of 4.1% and validated at a 4.2% level for the resistance, X'_T. In this case the data uncertainty is small, so validation at a higher level would require a finer grid, since this would reduce the numerical simulation uncertainty and consequently the validation uncertainty.

		E % D	U_V % D	U_D % D	U_{SN} % D
X'_T	$E = D - S$	0.4	4.2	0.9	4.1
	$E_C = D - S_C$	4.2	1.1	0.9	0.6

Table 12.1 Uncertainty for bare hull, $\beta = 0°$

Table 12.2 presents the results for the pure drift condition, $\beta = 4°$. For this condition the levels of verification for X'_T, Y'_T and N'_T are 4.3%, 8.3% and 2.7%, respectively. Validation is achieved at 6.3%, 9.3% and 6.3% levels for X'_T, Y'_T and N'_T, respectively and in order to validate at a higher level both the data and the numerical simulation uncertainties should be reduced.

		E % D	U_V % D	U_D % D	U_{SN} % D
X_T'	$E = D - S$	0.0	6.3	4.6	4.3
	$E_C = D - S_C$	3.4	4.7	4.6	1.0
Y_T'	$E = D - S$	5.7	9.3	4.3	8.3
	$E_C = D - S_C$	11.3	5.1	4.3	2.7
N_T'	$E = D - S$	1.7	6.3	5.7	2.7
	$E_C = D - S_C$	0.2	5.9	5.7	1.2

Table 12.2 Uncertainty for bare hull, $\beta = 4°$

Table 12.3 presents the results for the appended hull without propeller. For straight-ahead sailing with 0° rudder angle the resistance X_T' and the rudder drag X_{TR}' are verified at 0.4% and 32.3% levels, respectively. The two quantities are validated at 3.4% and 99.7% levels, respectively. For the resistance a reduction in the data uncertainty is required to validate at a higher level. The comparison error is quite high for the rudder force, so to identify possible modelling errors or obtain validation at a higher level both the data and the grid uncertainties should be reduced.

		E % D	U_V % D	U_D % D	U_{SN} % D
X_T'	$E = D - S$	0.1	3.4	3.4	0.4
	$E_C = D - S_C$	0.3	3.4	3.4	0.4
X_{TR}'	$E = D - S$	98.7	99.7	94.4	32.3
	$E_C = D - S_C$	122.8	94.7	94.4	8.3

Table 12.3. Appended hull, $\beta = 0°$, $\delta = 0°$

Table 12.4 presents the results for $\beta = 0°, \delta = -10°$. The forces X_T' and Y_T' are verified at 0.8% and 11.8% levels, respectively and validation is obtained at 3.4% and 28.0% levels, respectively. The yaw moment N_T' is verified to a level of 16.6%, but validation is not achieved. The rudder forces show that X_{TR}' and Y_{TR}' are verified at 73.2% and 11.4% levels, respectively and that validation is achieved at 80.1% and 13.1% levels, respectively. Again it is noted that the validation uncertainty should be reduced to obtain validation at higher levels and to identify modelling errors. Except for the resistance, this must be done by reduction of both the numerical and experimental uncertainties.

		E % D	U_V % D	U_D % D	U_{SN} % D
X_T'	$E = D - S$	0.8	3.4	3.3	0.8
	$E_C = D - S_C$	---	---	3.3	---
Y_T'	$E = D - S$	20.9	28.0	25.4	11.8
	$E_C = D - S_C$	10.0	25.4	25.4	1.0
N_T'	$E = D - S$	27.1	21.9	14.3	16.6
	$E_C = D - S_C$	16.5	14.4	14.3	2.0
X_{TR}'	$E = D - S$	21.9	80.1	32.6	73.2
	$E_C = D - S_C$	39.1	37.5	32.6	18.7
Y_{TR}'	$E = D - S$	5.9	13.1	6.5	11.4
	$E_C = D - S_C$	3.7	6.8	6.5	1.8

Table 12.4. Appended hull, $\beta = 0°$, $\delta = -10°$

Table 12.5 presents the results for the pure drift condition $\beta = 4°$, $\delta = 0°$. X_T' is not verified or validated due to grid divergence. Both Y_T' and X_{TR}' converge and verification is obtained at 5.4% and 84.4% levels, respectively, but validation is not achieved. N_T' and Y_{TR}' are verified at levels of 1.8% and 25.7%, respectively, and they are also validated at 6.5% and 37.2% levels, respectively. As in the previous cases the uncertainties should generally be reduced, but even without doing this, it is found that the comparison errors for both Y_T' and X_{TR}' were so high that they indicate the presence of a modelling error.

		E % D	U_V % D	U_D % D	U_{SN} % D
X_T'	$E = D - S$	0.8	---	4.6	---
	$E_C = D - S_C$	---	---	4.6	---
Y_T'	$E = D - S$	15.0	6.4	3.5	5.4
	$E_C = D - S_C$	18.4	4.0	3.5	1.9
N_T'	$E = D - S$	1.4	6.5	6.3	1.8
	$E_C = D - S_C$	0.4	6.3	6.3	0.8
X_{TR}'	$E = D - S$	267.9	155.2	131.4	84.4
	$E_C = D - S_C$	326.5	132.8	131.4	25.8
Y_{TR}'	$E = D - S$	18.4	37.2	26.9	25.7
	$E_C = D - S_C$	35.6	28.2	26.9	8.5

Table 12.5. Appended hull, $\beta = 4°$, $\delta = 0°$

Table 12.6 presents the results for the pure drift condition $\beta = 4°$, $\delta = 0°$, with propeller. X_T' is verified at a 0.8% level and validated at a 4.3% level. But, it is also found that even though verification is achieved at 3.7% and 3.4% levels for Y_T' and N_T', no validation is achieved for the two quantities. Concerning the rudder forces, the levels of verification for X_{TR}' and Y_{TR}' are found to be 11.1% and 1293.9%. X_{TR}' is not validated, and though the comparison error is smaller than the validation uncertainty for Y_{TR}', the levels of uncertainty are so high that it does not make sense to say that validation

is obtained. It must in this connection be mentioned that the zero rudder angle case is one of the most difficult conditions, since Y'_{TR} is very small and to a large degree depends on correct prediction of the pressure peak regions generated by the propeller swirl on the rudder surface.

		E % D	U_V % D	U_D % D	U_{SN} % D
X'_T	$E = D - S$	2.3	4.3	4.2	0.8
	$E_C = D - S_C$	2.3	4.2	4.2	0.2
Y'_T	$E = D - S$	13.7	5.1	3.5	3.7
	$E_C = D - S_C$	15.8	3.9	3.5	1.6
N'_T	$E = D - S$	14.3	6.6	5.6	3.4
	$E_C = D - S_C$	---	---	5.6	---
X'_{TR}	$E = D - S$	35.6	18.3	14.5	11.1
	$E_C = D - S_C$	43.1	15.5	14.5	5.4
Y'_{TR}	$E = D - S$	5.45	1294.3	30.1	1293.9
	$E_C = D - S_C$	95.3	403.0	30.1	401.9

Table 12.6. Appended hull with propeller, $\beta = 4°$, $\delta = 0°$

The verification and validation described in this section were only performed for selected conditions, so in order to study the CFD code's ability to predict the behaviour of the computed forces over a range of conditions, they are plotted together with the experimental data in Section 13. For the bare hull, the computation and the experiment generally agree well both quantitatively and qualitatively. When the rudder is included without the propeller, the measured and computed overall forces qualitatively follow the same trends. But, quantitatively slight discrepancies are observed between the two sets of data. Concerning the rudder forces, larger deviations are observed. The rudder drag seems to be somewhat over-predicted by the computations for both straight-ahead and oblique flow conditions. The lift is found to be most difficult to compute for the oblique flow condition. When the propeller is included, the computation generally captures the overall behaviour of the forces and moments, but again quantitative differences are observed.

12.2. Field level quantities

The verification and validation of field level quantities is documented in References /4/ and /8/.

The verification of the field quantities was carried out for velocity profiles along horizontal cuts in the wake of the ship, at X/L = 1.025, Z/L = -0.015, -0.030, -0.0463 and –0.062, as shown in Figure 12.1.

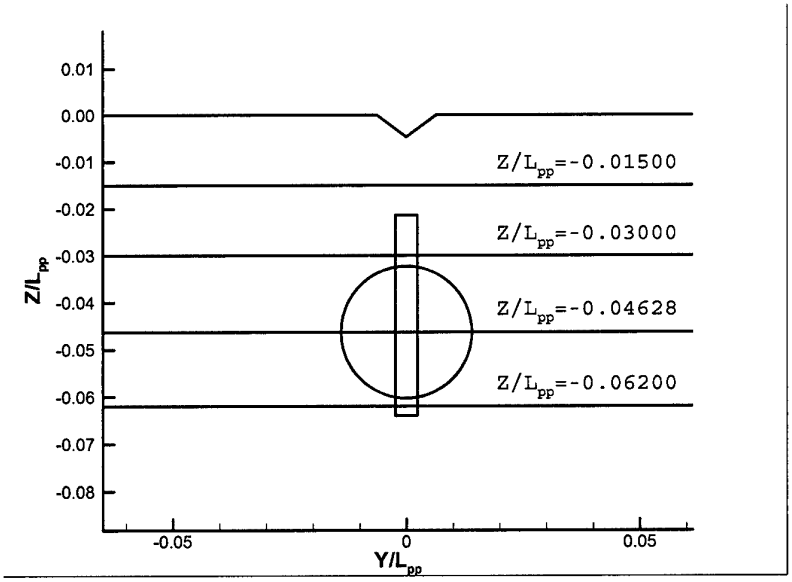

Figure 12.1. Lines where velocity profiles are considered.

The verification was performed for four different conditions: straight-ahead with zero rudder angle, i.e. $(\delta,\beta)=(0,0)$, static rudder with $(\delta,\beta)=(-10,0)$, pure drift with $(\delta,\beta)=(0,4)$ and straight-ahead with propeller, i.e. $(\delta,\beta)=(0,0)$.

Based on the results of the verification, it was found that the correction factor C_G calculated on the basis of $\langle p_G \rangle$ were in the range from 0.4 to 3.7. The correction factor indicates how close the solution is to the asymptotic range and consequently if the solution should be corrected for numerical errors. C_G close to unity indicates that the solution is in the asymptotic range and that the solution should be corrected for the numerical error. However, since there is no clear concentration around 1 for the present C_G values, the solutions are not corrected for numerical errors, so only the uncertainty is considered.

To illustrate, selected profiles for the pure drift condition are plotted in Figure 12.2. The figure shows that the uncertainty distribution over the profile varies and that the highest uncertainties are located in the centre plane wake.

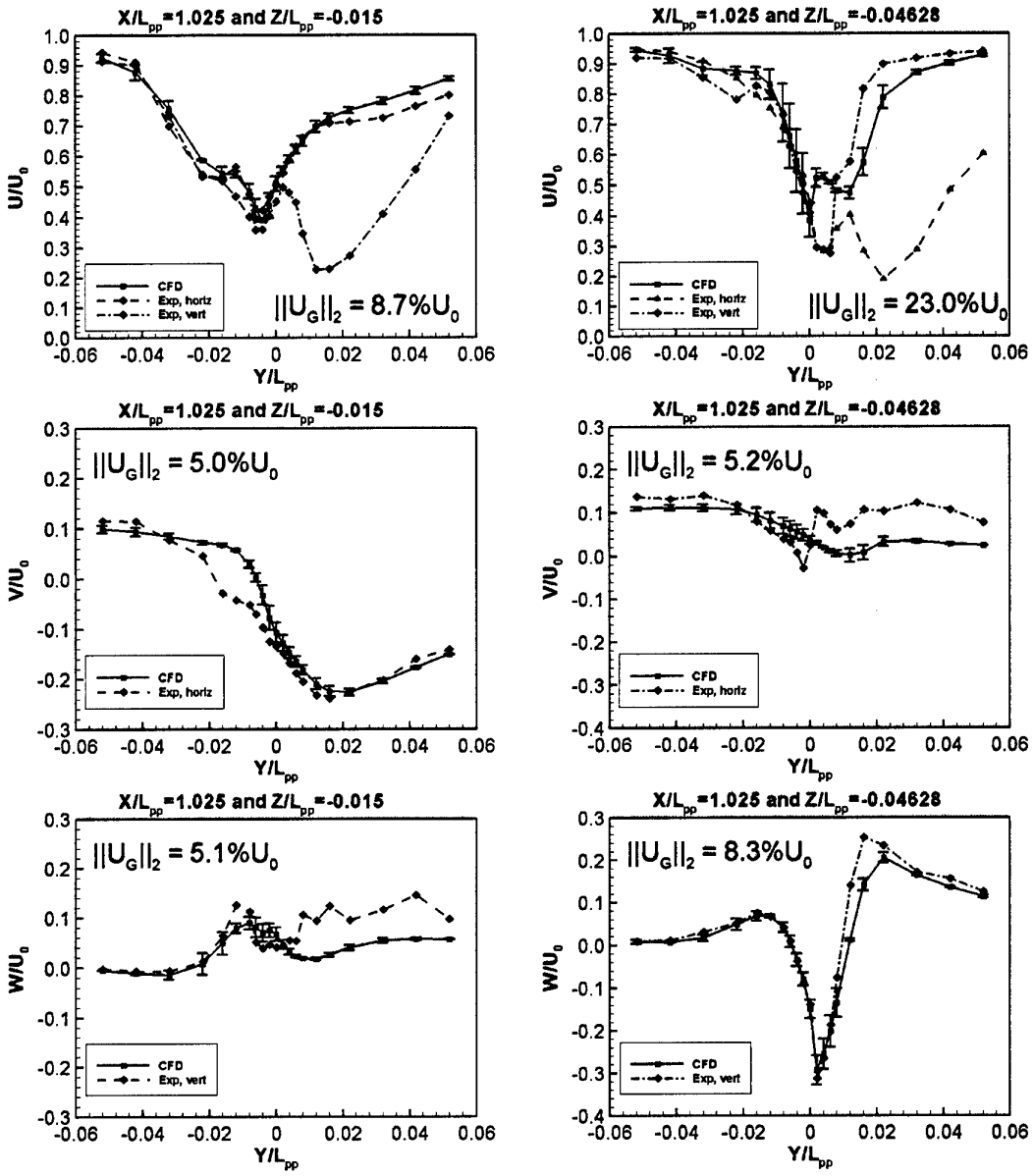

Figure 12.2 Computed and measured velocity profiles plus grid uncertainty for β=4°

Tables 12.7 through 12.9 show the simulation uncertainty for the four profiles for each of the three manoeuvring conditions. It is seen that for straight-ahead and static rudder the uncertainty related to U is of the same order of magnitude, while it is somewhat larger for the pure drift condition. For V the uncertainty for static rudder and pure drift mainly appears to be a little higher than for straight-ahead. The same happens for W, but in this case the pure drift uncertainties are also higher than the static rudder case. It appears that the increase in the uncertainty correlates with the complexity of the flow pattern. However, this makes sense because when the same grid resolution is used for all three conditions it is most likely that the most complex condition is the most difficult to resolve, which lead to the highest simulation uncertainty. In order to reduce the simulation uncertainty finer grids should be used. As mentioned earlier the iterative uncertainty is neglected. The reason is that U_I generally is 10 to

20 times smaller than U_G. For example $\|U_I\|_2$ is 0.40%U_0, 0.24%U_0 and 0.31%U_0, for U, V and W, respectively, for the pure drift condition, along the line at $Z / L_{pp} = -0.015$.

Z/L_{pp}	-0.01500	-0.03000	-0.04628	-0.06200
U	5.7 %	10.3 %	15.2 %	7.9%
V	3.2 %	2.1 %	10.5 %	2.5 %
W	5.2 %	6.1 %	3.5 %	2.6 %

Table 12.7. $\|U_{SN}\|_2$ in % of U_0 for Straight-ahead

Z/L_{pp}	-0.01500	-0.03000	-0.04628	-0.06200
U	5.5 %	10.4 %	14.3 %	9.0 %
V	7.4 %	3.7 %	29.1 %	2.9 %
W	4.9 %	7.0 %	6.5 %	2.9 %

Table 12.8. $\|U_{SN}\|_2$ in % of U_0 for Static rudder

Z/L_{pp}	-0.01500	-0.03000	-0.04628	-0.06200
U	8.7 %	14.8 %	23.0 %	28.3 %
V	5.0 %	4.0 %	5.2 %	5.4 %
W	5.1 %	7.5 %	8.3 %	5.0 %

Table 12.9. $\|U_{SN}\|_2$ in % of U_0 for Pure drift

After analysing the measured PIV data it turned out that the quality was not as good as hoped for. The problem is illustrated in 12.2, which shows U, V and W data measured at two different Z-locations in the wake with $\beta = 4°$. At $Z / L_{pp} = -0.015$ on port side the U components measured in the vertical and horizontal planes are in fair agreement, but on starboard side, where the main vortex is located, the vertical plane U velocity is far lower than the horizontal plane velocity. At $Z / L_{pp} = -0.04628$ the opposite is observed, i.e. the horizontal plane U velocity is smaller than vertical plane U. The lack of reproducibility on starboard side is most likely related to the fact that the PIV technology is quite sensitive to the magnitude of the velocity component going through the measuring plane in the normal direction. This means that when the U and V components are measured in the X-Y plane the results are not as good if the vertical W component going through the plane in the Z-direction is too strong. The same happens if the V component is too strong when U and W are measured. If the problems are caused by this effect, it means that horizontal data should be used at $Z / L_{pp} = -0.015$ where the cross flow is V dominated, while the vertical plane data should be used at $Z / L_{pp} = -0.04628$ where the flow is W dominated. With the available experimental data it is difficult to conclude about the data quality. Therefore, the simulated and measured will be compared qualitatively instead of quantitatively.

Based on an overall qualitative comparison of the experimental and computational wake data for the different manoeuvring conditions regions of good and poor agreement can be identified. For pure drift, both sets of data show the velocity defect and the asymmetry introduced by the oblique flow. Though, the agreement varies depending on the location in the wake field. A pattern appears, where the calculated distribution and magnitude of (U, V, W) qualitatively agree with the measurement on port side,

while differences are observed on starboard side, where the main vortex is located. In the upper wake the calculation agrees with the horizontal plane (U, V), but not with the vertical plane (U, W). In the lower wake, the opposite happens, which makes it possible to see the presence of the vortex. Figure 12.2 illustrates the typical magnitude of the deviations. However, assuming that the data problems are caused by the problem described above, the computation is in agreement with the data that are considered valid.

For the straight-ahead condition the measurement was only performed on starboard side, so it is not possible to see the symmetry of the flow field, but the wake deficit can be observed in the U component. Further, the presence of the bilge vortex can be seen in the vertical velocity component, W, which in the lower wake agrees with the computation. The agreement between the measured and computed V component is not evident, except in the upper part of the wake, where the inboard directed flow is strong. With respect to the regions where agreement between experiment and computation is achieved, straight-ahead shows the same pattern as pure drift.

The static rudder condition is not particularly different from the straight-ahead case, when it comes to the comparison. Again the wake deficit is observed in U, but in addition to this the asymmetry introduced by the deflected rudder can also be seen. The computation agrees with horizontal plane data in the upper wake and with the vertical plane data in the lower wake, where the presence of the bilge vortex is seen.

Seen in relation to flow study presented later, the validation indicates that the magnitude and distribution of the calculated velocity components to a certain degree look reasonable for the considered conditions. But, since the two cross-flow components (V, W) could not be measured at coinciding locations, it is not possible to map the vortices and the vorticity, which means that the vortex tracking cannot be validated properly

13. Results: Integral level Quantities

13.1. Bare hull, appended hull in pure drift, static rudder

The computed and measured forces and moments for the bare hull in static rudder and pure drift are shown in Figures 13.1 (a) and (b), together with the data and simulation uncertainty bands for the two cases considered for V&V in the sections above. Overall the computation captures the trends in the data, but has a tendency to slightly under-predict the force and moment compared to the experiment. The under-prediction appears to be strongest for the larger angles, which is not unexpected, since the flow becomes more complex and difficult to model, due to increased cross-flow around the hull and formation of strong vortices.

Figures 13.1 (c), (e) and (g) present the measured and computed forces and moments acting on the complete hull-rudder system in the static rudder condition, together with the experimental data and the numerical simulation uncertainty bands from the V&V described above. The forces acting locally on the rudder, X'_{TR} and Y'_{TR}, are presented in Figures 13.2 (a) and (c). These results demonstrate that the CFD method qualitatively captures the behaviour of the considered forces and moments in the static rudder case. But there are some quantitative differences which cannot be explained satisfactorily without reducing the numerical and experimental uncertainties. If this is done it may be possible to estimate the modelling errors, which for example may originate from the transition in the rudder boundary layer, the missing rudderstock in the numerical model or the missing effect of the free surface.

The computed and measured forces and moments, plus the levels of data and numerical simulation uncertainty from the V&V, are shown in Figures 13.1 (d), (f) and (h) for the appended hull in the pure drift condition. The local rudder forces X'_{TR} and Y'_{TR} are shown in Figures 13.2 (b) and (d), respectively, together with the levels of uncertainty found in the V&V cases, $\beta = 0°$ and $\beta = 4°$. From the results it appears that the CFD code qualitatively captures the behaviour of the total forces and yaw moment. But with respect to the quantitative agreement the picture is a little more complex.

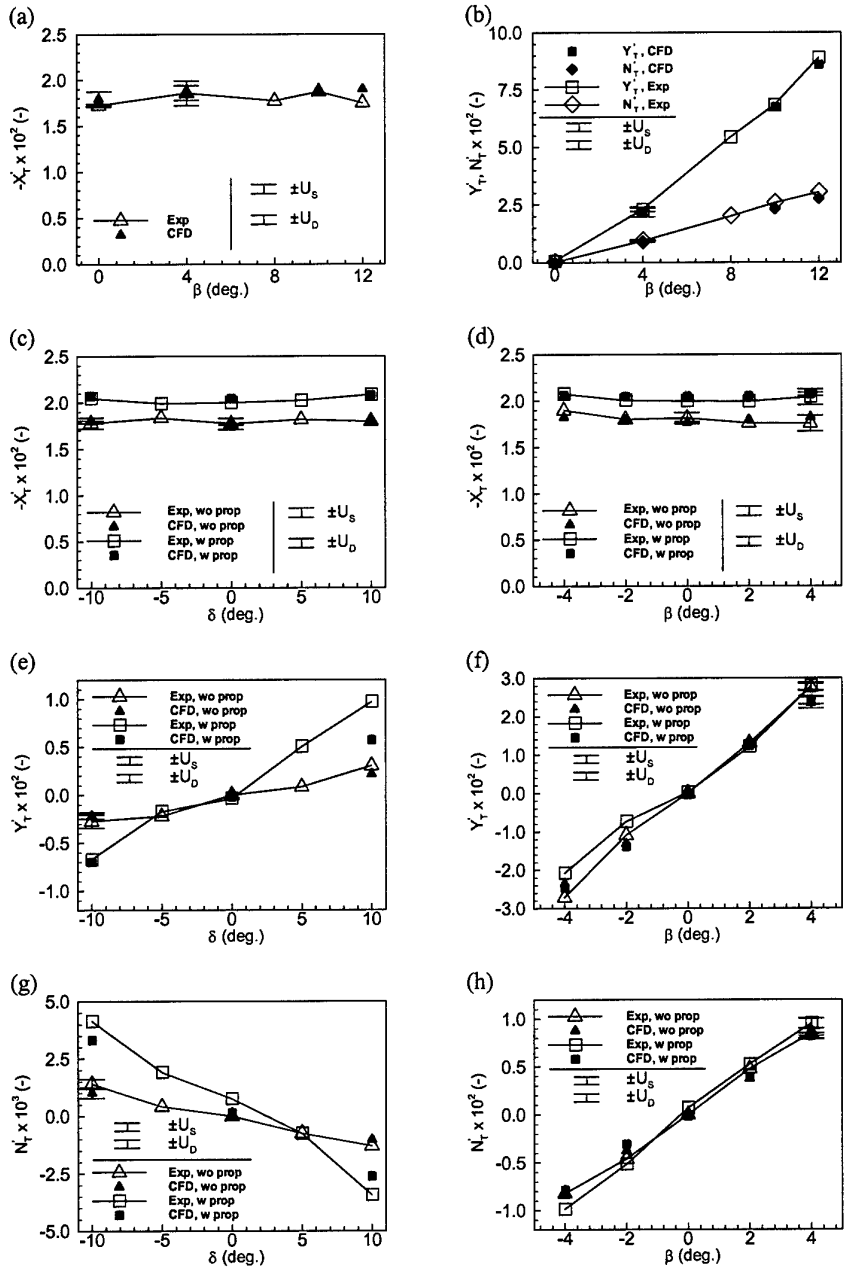

Figure 13.1. Calculated and measured global forces and moment acting on hull and rudder. Bare hull: (a) and (b). Appended hull, static rudder: (c), (e) and (g). Appended hull, pure drift: (d), (f) and (h)

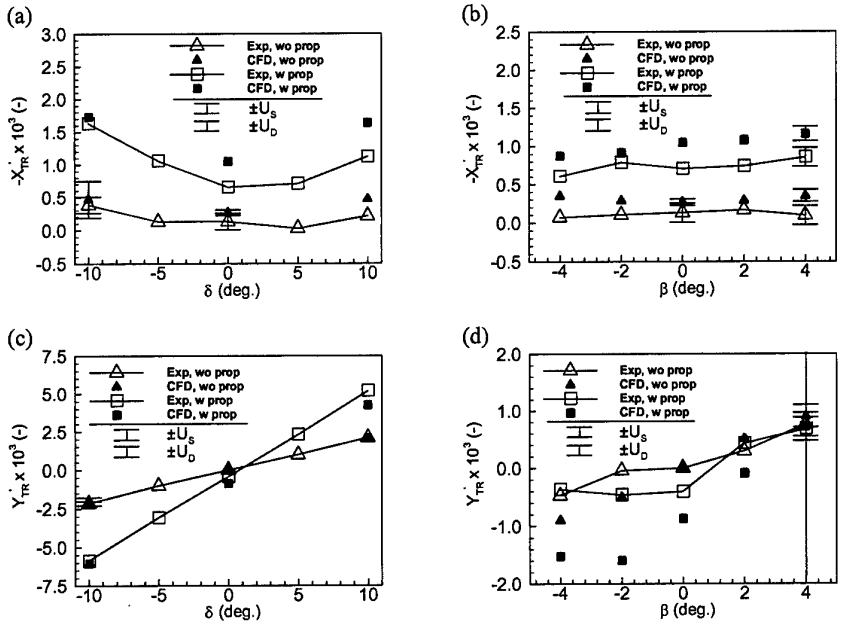

Figure 13.2. Calculated and measured rudder forces: static rudder (a) and (c), pure drift (b) and (d)

Computing the rudder forces is apparently more difficult. The rudder forces in the considered case are small and therefore difficult to measure accurately, but it must also be kept in mind that a good numerical rudder force prediction depends not only on the correct modelling of flow near the rudder itself, but also on the correct modelling of the ship wake flow, in order to provide the correct inflow field to the rudder. In order to clarify this, a detailed study of the flow field is required, together with verification and validation of the flow field.

13.2. Lifting line propeller – Series 60

The results for the lifting line propeller model are documented in References /6/ and /9/, and summarised herein.

Figure 13.3 shows the convergence history of the thrust and torque for the lifting line propeller model on the Series 60 hull. It is seen that both thrust and torque converge as the number of iterations is increased. K_T and K_Q decrease between the nominal wake solution (iteration 0) and the subsequent effective wake solutions, and convergence is obtained relatively rapidly during the next two or three iterations. The decrease in thrust and torque is explained by the fact that the propeller is more heavily loaded in the undisturbed nominal wake field than in the effective wake field, where the magnitude of the inflow velocities are higher. The difference between the nominal and effective conditions can also be seen directly in the local propeller loading, i.e. in the applied body-forces, Figure 13.4 (a) and (b), since the forces decrease when going from the nominal to the effective solution. It should be noted, that the body-forces does not appear to be distributed completely smoothly. The reason is that the RANS grid is not cylindrical, which means that the round disk is resolved by a H-grid topology. This problem is not present in the later *Esso Osaka* simulations (see Section 13.3), since a cylindrical grid block is used in the propeller region in this case.

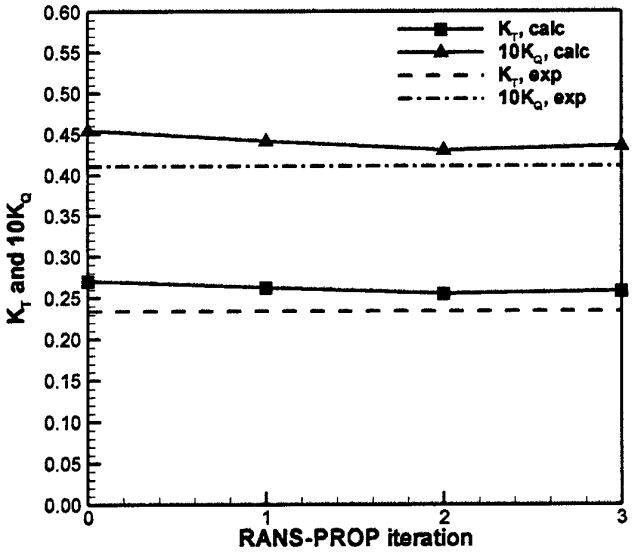

Figure 13.3 Convergence history for lifting line propeller on Series 60

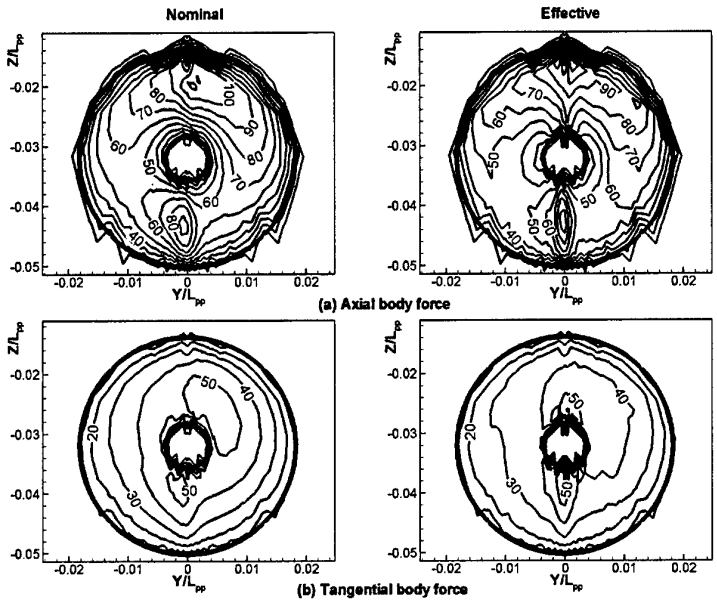

Figure 13.4 Propeller body forces for lifting line propeller on Series 60

The calculated K_T and K_Q, are shown in Table 13.1, together with experimental data from Reference /15/. From the table it is seen that the applied propeller model over-predicts both thrust and torque. The thrust is predicted within 9.8% of the measured value, while the torque is predicted within 5.8%.
Two other quantities that are relevant to consider in connection with the hull-propeller configuration are the wake fraction, w and the thrust deduction factor, t. The wake fraction is defined by

$$(1-w)=\frac{J_a}{J_0}=\frac{U_a}{U_0}$$

where J_a and $J_0 = 0.88$ are the advance coefficients, $J = U / nD_p$, based on advance, U_a and ship U_0 speeds, respectively. (1-w) can be determined in two ways. The first method is based on a thrust identity, (T. ID.), where J_0 and J_a are used. J_a is obtained from the open water propeller curve as the J value corresponding to the thrust measured during the test with the propeller running behind the ship. The second method is to use U_0 and U_a, where U_a is calculated by averaging the wake field over the propeller disk. The thrust deduction factor is defined by

$$(1-t)=\frac{X_{WO}-F_D}{T}$$

where X_{WO} is the ship resistance without propeller, T is the propeller thrust and F_D is the relaxation force, which expresses the difference in frictional coefficients between model and full scale.
With respect to the effective wake fraction, (1-w), Table 13.1 shows the values obtained by the thrust identity method and averaged wake velocity method and it is seen that the two methods agree fairly well. However, the table also shows that the calculation under predicts the quantity compared to the experiment, but this makes sense since the thrust is over predicted. Concerning the thrust deduction factor, (1-t), the ship is sailing at the model scale self-propulsion point, i.e. $F_D = 0$ so the above expression for (1–t) reduces to $(1-t) = X_{WO} / T$. However, by using this expression, the resistance for the model, found without free surface, is related to propeller settings found when including the free surface. Therefore, to give a better idea about the suction on the hull from the propeller, the following definition of (1-t) could be used, $(1-t) = X_{WO} / X_W$, which means that (1-t) is the ratio between the resistance without and with propeller. According to Table 13.2 the agreement is fair when the computation is compared with the experiment. This indicates, that the propeller model gives the right amount of suction on the hull upstream of the propeller.

Case 1	K_T	$10K_Q$	(1-w) T. ID.	(1-w)	(1-t)
Exp.	0.234	0.411	0.75	---	0.86
Calc.	0.257	0.435	0.69	0.68	0.85

Table 13.1 Measured and calculated propeller quantities

Based on the results for the Series 60, the results obtained with Yamazaki's propeller model are encouraging. The measured and calculated propeller quantities differ somewhat, but this may to some point be explained by the representation of the propeller disk in the RANS grid, which could be improved by using cylindrical grids. Further, the agreement between measured and calculated field quantities is fair behind the propeller, which is important for the following simulations, where the rudder is included behind the propeller.

13.3. Lifting line propeller – *Esso Osaka*

The RANS-propeller code convergence for the *Esso Osaka* calculations is illustrated in Figure 13.5, which shows the convergence history of the propeller coefficients in straight-ahead sailing. Both thrust and torque converge as the number of iterations increases, and it should be noted that the convergence history looks the same for all three conditions. Five iterations are required in order to reduce the changes in the propeller coefficients between iterations to less than one percent. For the same reason as

described for the Series 60 model, K_T and K_Q decrease between the nominal wake solution (iteration 0) and the subsequent effective wake solutions. The difference between the nominal and effective conditions can be seen in the local propeller loading, which is illustrated in Figure 13.6.

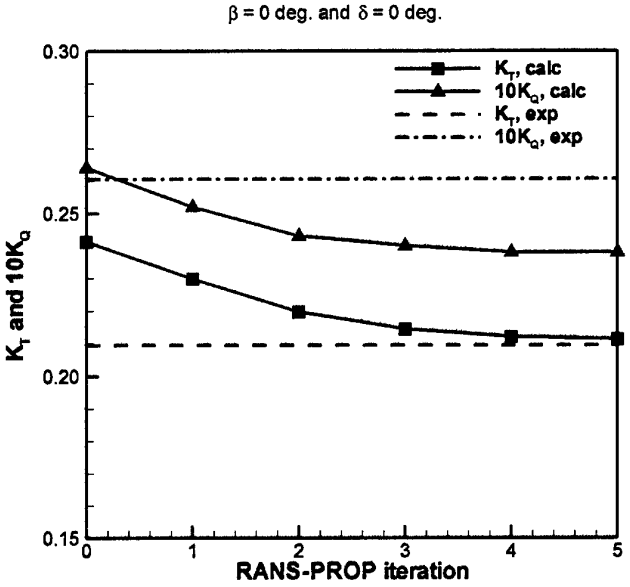

Figure 13.5 Convergence history for lifting line propeller on Esso Osaka

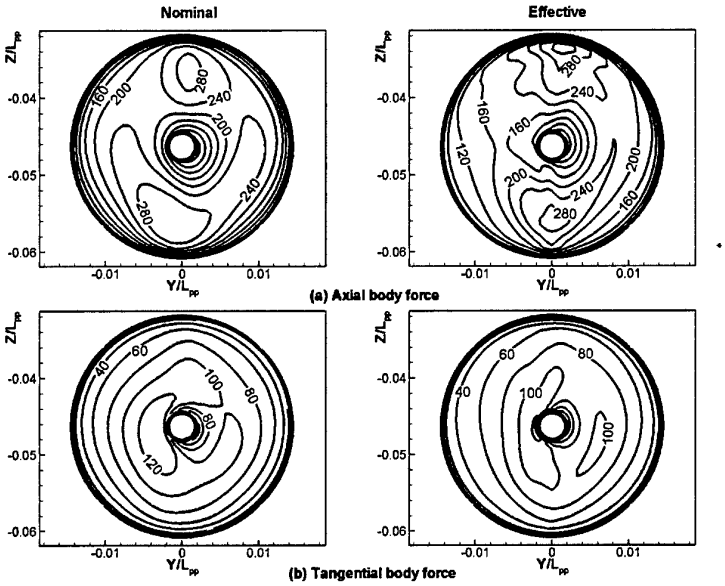

Figure 13.6. Propeller body-forces for lifting line propeller on *Esso Osaka*

The calculated thrust and torque for the straight-ahead condition are shown in Table 13.2, together with experimental data measured in FORCE Technology's towing tank. From the table it is seen that the applied propeller model predicts the thrust fairly well, while the torque is somewhat over predicted. The thrust is predicted within 0.5% of the measured value, while the torque is predicted within 8.8%. For the static rudder case, the thrust and torque are predicted within 1.9% and 2.4% of the measured values, respectively. Finally Table 13.4 shows that K_T and K_Q for pure drift are predicted within 4.9% and

3.2% of the experimental values. It appears that the calculation has a tendency to over predict the thrust and under predict the torque, when compared to the experimental data.

Case 2	K_T	$10K_Q$	$(1-w)$ T. ID.	$(1-w)$	$(1-t)$
Exp.	0.210	0.261	0.47	---	0.79
Calc.	0.211	0.238	0.46	0.43	0.75
Diff. %	0.5	8.8	2.1	---	5.1

Table 13.2. Measured and calculated propeller quantities, $\beta = \delta = 0°$

Case 3	K_T	$10K_Q$	$(1-w)$ T. ID.	$(1-w)$	$(1-t)$
Exp.	0.214	0.249	0.45	---	0.76
Calc.	0.218	0.243	0.43	0.43	0.69
Diff. %	1.9	2.4	4.4	---	9.2

Table 13.3. Measured and calculated propeller quantities, $\beta = 0°$, $\delta = -10°$

Case 4	K_T	$10K_Q$	$(1-w)$ T. ID.	$(1-w)$	$(1-t)$
Exp.	0.204	0.249	0.49	---	0.74
Calc.	0.214	0.241	0.45	0.46	0.73
Diff. %	4.9	3.2	8.2	---	1.4

Table 13.4. Measured and calculated propeller quantities, $\beta = 4°$, $\delta = 0°$

The effective wake fraction, $(1-w)$ for straight-ahead, static rudder and pure drift are shown in Tables 13.2 to 13.4, respectively. As for the Series 60 ship, $(1-w)$ is both calculated by means of the thrust identity and averaged wake field. A comparison between the two methods reveals fair agreement, even though the trust identity estimate is a little higher than the averaged approach for the straight-ahead condition. When compared to the experiment, fair agreement is also observed and the smallest deviation is found for the straight-ahead condition, while the biggest is observed for pure drift. The calculation generally seems to over predict $(1-w)$, but this is a result of the over prediction of the thrust, which is observed in all the considered cases.

The thrust deduction factor, $(1-t)$ is also shown in the three tables. It should be noted that in this case, the simulation is conducted with relaxation, i.e. $F_D \neq 0$. This is done by using the propeller settings from the experiment, which was conducted with relaxation according to standard test procedures. Further, the free surface effects are assumed to be small. Therefore, $(1-t)$ is calculated including F_D. According to the tables, the calculated data looks fair. The best agreement is obtained for pure drift, while the worst is found for the straight-ahead condition. When relating the quality of the agreement between calculation and experiment to the thrust one would expect to see best agreement for straight-ahead and worst for pure drift. However, this is not the case and the reason is that, as documented in Reference /7/ the without-propeller resistance also deviates from the experimental data leading to additional errors.

14. Results: Field level quantities

14.1. Velocities and pressures on bare hull and appended hull

14.1.1. Axial velocity for straight-ahead and static rudder

The U contours for $\beta = \delta = 0°$ are shown in Figure 14.1 (a) and (b). The flow field is similar to those reported for other full-form ships, e.g., the full form KVLCC: the flow is symmetric and a stagnation zone is located in the bow region. Downstream of this zone, the flow is accelerated around the shoulders and bilges of the ship. A thin boundary layer builds up along the hull and when it reaches the location where the hull begins to narrow in, the thickness increases rapidly and the wake field with bulging velocity contours is formed. The flow is retarded over a relatively large portion of the wake region, which means that the rudder operates in a flow field where the axial velocity is less than half of the ship speed. When compared with the corresponding bare hull flow (not shown here), the influence of the rudder on the flow is weak and local, since a very thin boundary layer builds up along the rudder surface and the flow is slightly accelerated. When the rudder is turned, $\delta = -10°$, the stern flow loses its centreplane symmetry, as shown in Figure 14.1 (c) and (d). Compared to $\delta = 0°$ the two flows are similar except in the vicinity of the rudder: in the wake right behind the rudder, the contours are more twisted, since high-velocity fluid is dragged into the port side of the wake. Further, the flow is accelerated on the port (low-pressure) side and retarded on the starboard (high-pressure) side.

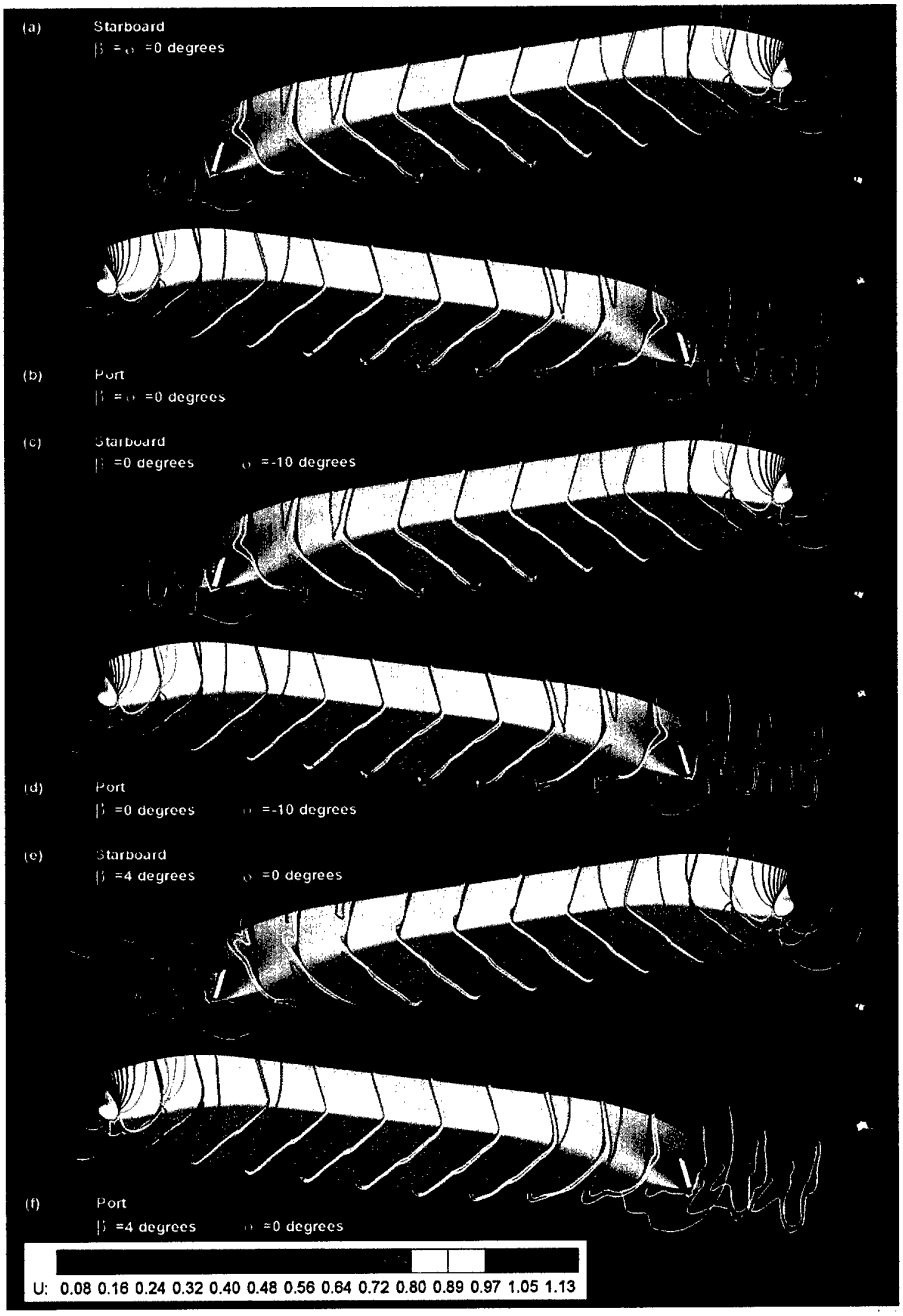

Figure 14.1 Axial velocity contours for straight-ahead , static rudder and pure drift conditions

14.1.2. Cross-flow velocity for straight-ahead and static rudder

The axial vorticity reveals a vortex system consisting of six vortices, as shown in Figure 14.2 (a) and (b). In the bow, two symmetric outboard counter-rotating fore body bilge vortices (FBV) are generated when the fluid is forced downward around the fore body bilges. The two vortices run along the bottom of the ship where they gradually move towards the bilges and away from the bottom with increasing *X*. The vorticity is high in the bow region and decays relatively rapidly with increasing *X*. The axial velocity

component in the vortex core is low in the beginning, but it increases gradually as X increases and the vortex core moves out of the boundary layer. The vortex disappears around X=0.7.

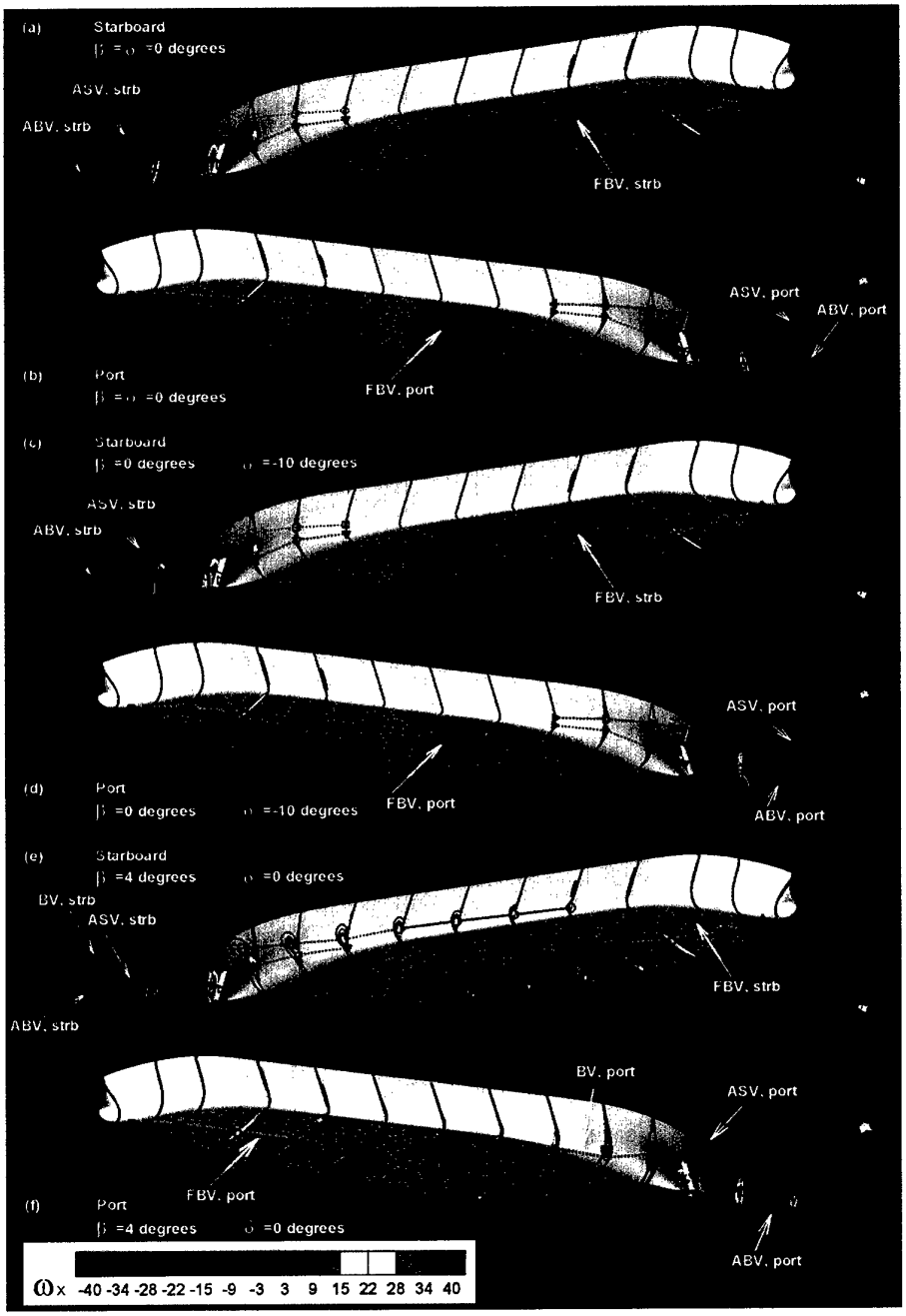

Figure 14.2 Axial vorticity for straight-ahead, static rudder and pure drift

The next vortices are the two symmetric inboard counter-rotating aft body bilge vortices (ABV), which cause the hook shape of the wake contours. The two vortices develop around the bilges in the aft ship. They originate around X≈0.7 where the hull form is narrowing in and where the fluid particles, which have been forced below the bottom, start to move upwards and around the bilges. The vortices run along the lower part of the stern before they continue into the centreplane wake where they pass the rudder and end up in the far wake behind the ship. The vorticity first increases with the X-location before it gradually

decays with increasing X behind the ship. Since the trajectories run through the centreline wake they experience a relative small velocity. The core axial velocity decreases until it reaches a minimum at approximately X=0.95, after which it recovers to increase with distance behind the ship.

The final two vortices are the symmetric outboard counter–rotating aft body side vortices (ASV). It was previously found that they exist behind the KVLCC but not behind the Series 60 ship. According to Figure 14.2 (a) and (b) the two vortices can be found behind the Esso Osaka. They begin to build up at the same X-location as the ABVs, but they follow a path along the side towards the water surface. The vortices are relatively weak. ω_X first increases slightly along the hull and then decreases behind the ship. The axial velocity in the vortex core for ASV behaves as the ABV, though the velocity deficit is less pronounced for the ASV.

When the rudder is deflected, the vortex system is quite similar to the $\beta = \delta = 0°$ case, as shown in Figure 14.2 (c) and (d). The following local differences are found in the stern region: The flow gets asymmetric. The rotational flow disappears in the ASVs. The ABV moves upwards on starboard side and slightly downwards on port side. The strength of the ABVs on the port side increases over the rudder and behind the ship, while it decreases on starboard side. For the ASVs the opposite behaviour is observed. The axial velocity in the core of the port side ASV does not change much whereas it increases on starboard side. For the port side ABV the flow is first accelerated over the rudder, but downstream of the rudder the velocity decreases again. The opposite behaviour is observed for the starboard side ABV.

14.1.3. Pressure distribution for straight-ahead and static rudder

As shown in Figure 14.3 (a) and (b), the pressure distribution on the hull and rudder surfaces for $\beta = \delta = 0°$ is symmetric. In the bow a high-pressure region is observed due to stagnation. Progressing downstream, the pressure decreases strongly over the shoulders, which correlates with the high velocity region described earlier. Further downstream the pressure increases to a constant but slightly negative level until it reaches the X-position where the hull starts to narrow in again. Downstream of this position the pressure again decreases slightly before it starts to recover in order to become positive at the stern. The lowest pressure in the stern occurs in the aft body bilge region, which correlates with acceleration of the flow around the bilges

A comparison with the bare hull data for the straight-ahead condition (not shown) reveals that the presence of the rudder locally increase the pressure symmetrically on both port and starboard sides of the hull. On the rudder itself, the pressure field is shown in more detail in Figure 14.6, in connection with the discussion of propeller effects on the local rudder pressures. As shown in Figures 14.3 and 14.6, the pressure on the rudder varies in both chordwise and spanwise directions. In the chordwise direction, the pressure is high at the leading edge due to stagnation. Downstream of this region, the pressure first decreases due to the thickness of the rudder before it recovers towards the trailing edge. In the spanwise direction the pressure is low on the lower half of the rudder, but it increases on the upper part. This behaviour correlates with the presence of the two inboard rotating ABVs, which direct the flow towards the upper part of the rudder.

Turning the rudder to $\delta = -10°$, leads to the pressure fields shown Figure 14.3 (c) and (d). On the rudder itself, the pressure field is shown in more detail in Figure 14.7, in connection with the discussion of propeller effects on the local rudder pressures. In spite of some similarity, the surface pressure on both hull and rudder does change compared to $\delta = 0°$. A slight port-starboard asymmetry is observed on the hull, but the most radical changes occur on the rudder itself. The pressure generally increases on starboard side, and a peak is observed at the leading edge close to the gap between the rudder and the hull. The overall increase of the pressure correlates with the fact that starboard side of the rudder is the pressure side and the observed peak is a result of the interaction between rudder and hull. On port side of the rudder, i.e. the suction side, the pressure decreases. The behaviour of the pressure field correlates with the acceleration and deceleration of the flow on port and starboard sides, respectively.

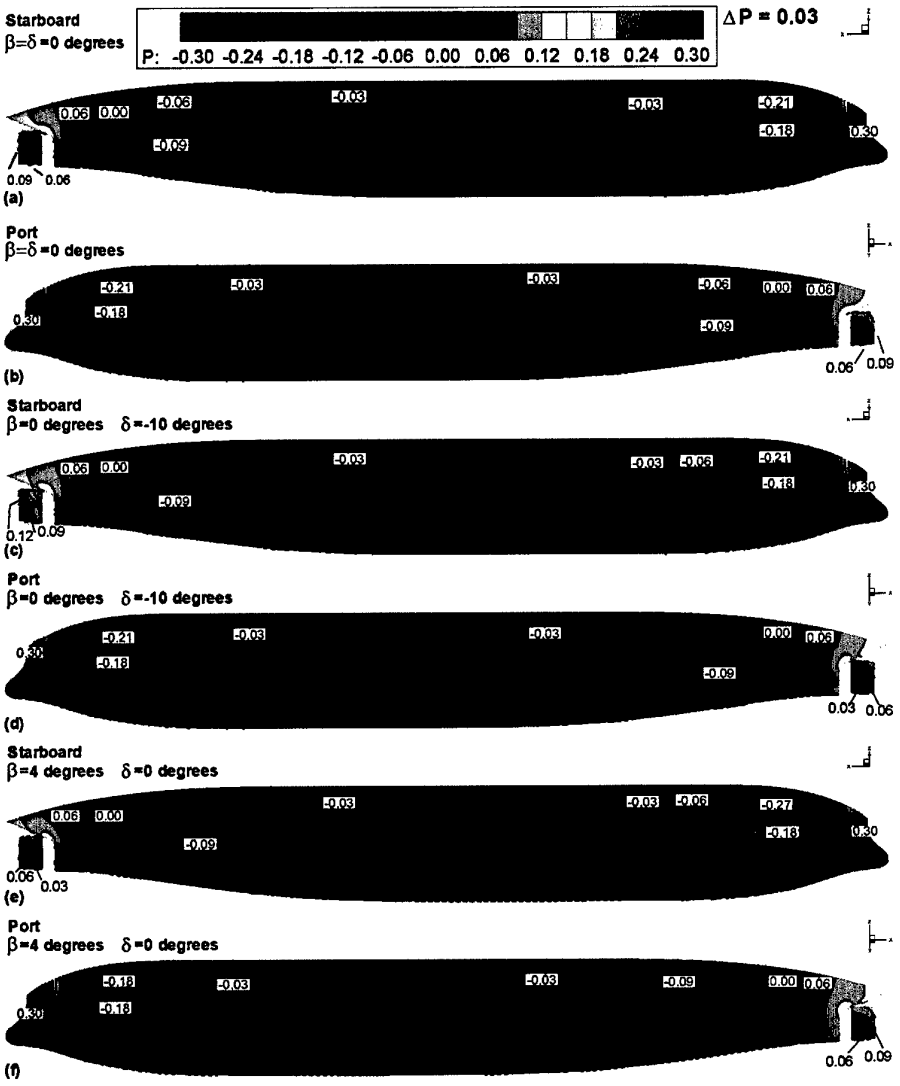

Figure 14.3 Pressure distribution on hull and rudder

14.1.4. Axial velocity in pure drift

The drift calculations cover the bare hull with $\beta = 4°$ and $\beta = 10°$, plus the appended hull with $\beta = 4°$. The results for the appended hull are summarised herein. Figure 14.1 (e) and (f) show the axial velocity for the condition, $\beta = 4°$ and $\delta = 0°$. The flow is no longer symmetric. On the port (windward) side of the bow, the extent of the stagnation zone is increased compared to the straight-ahead case, leading to a larger region with low axial velocity. On the starboard (leeward) side of the bow, the flow is accelerated more than in the straight-ahead case. The boundary layer still develops along the hull. It is thinner on the windward side than on leeward side, and it appears that the asymmetry increases with increasing drift angle. Further, there is a local thickening of the boundary layer in the region close to starboard bilge and on the port side of the bottom of the ship. The explanation is found in two bilge vortices, which develop when $\beta \neq 0°$. With respect to the wake itself, it is significantly different from the straight-ahead case. On the windward side, the velocity contours are smoother, i.e. the inner wake hooks disappear and the wake

is thinner. On leeward side, the hooks are more pronounced and the low velocity region extends further into the far field. If the flow field is compared with the corresponding bare hull results, the main difference between the two configurations is that the rudder splits the contours at the rudder position, where a thin rudder boundary layer is allowed to develop. Further, the velocity is slightly higher in the lower part of the wake downstream of the rudder.

For $\beta = 4°$, the vortex system shown in 14.2 (e) and (f) develops. Compared to the straight-ahead case the six vortices are still present as peaks in ω_X. The vortex pattern is not symmetric, however, since the extent of the regions with circulating flow and the trajectories of the vortices are different. Further, two additional vortices appear along the bilges. However, starting with the FBVs, the two vortices move towards the starboard side, due to the drift-induced cross flow around the bottom of the ship. It is not evident in the present figures, but the bare hull data show that the transverse displacement increases with the drift angle. Further, the longitudinal extent of the region with circulating flow decreases for both vortices. The reduction is most pronounced for the starboard FBV. As for the straight-ahead condition the vortices are strong at the bow and decrease with increasing X. Relative to that condition the strength increases and decreases on port and starboard sides, respectively. The reason is that the direction of the drift-induced cross flow helps drive the port side vortex, while it counteracts the starboard vortex. With respect to the axial core velocity, U/U_0 on the port side is generally lower than for straight-ahead, and a reduction occurs between $X/L_{pp} \approx 0.2$ and $X/L_{pp} \approx 0.4$. On the starboard side the picture is more difficult to characterise, but it seems that U/U_0 is low in the beginning and then increases with X in the downstream direction. In the ABVs, which dominate the straight-ahead case, the circulating flow in the vortex on port side disappears behind the ship, leaving the starboard ABV as the main vortex. When the vortex is still running along the hull, the opposite situation is found. With respect to the axial velocity component the velocity deficit is also present for $\beta \neq 0°$, the minimum velocity in the deficit region around $X/L_{pp} \approx 1$ appears to be a little higher than for $\beta = 0°$. Further, the velocity on port side appears to be lower than on starboard side. With respect to the ASVs, the rotation in the vortices more or less disappears when $\beta \neq 0°$. The final two vortices to be discussed are the co-rotating bilge vortices (BV), which develop when $\beta \neq 0°$. The vortices develop at the bilges along the hull and continue into the wake behind the ship, as shown in Figure 14.2. They are both generated when the oblique flow forces the water around the bilges. The starboard BV runs along the lower part of the starboard side, while the port BV runs along the port side of the bottom. Due to the oblique flow, the port side BV is forced into the centreline wake, while the starboard side BV is forced away from the wake and into the far field. Bare hull data show that the transverse displacement increases with the drift angle and that the axial vorticity increases with the drift angle for both vortices. The highest vorticity occurs on port side. Both vortices are strong in the fore part of the ship, but they loose their strength relatively rapidly in the downstream direction. The axial core velocity first increases along the hull, then decreases slightly in the wake region around $X/L_{pp} \approx 1$ before it recovering further downstream of the ship.

The presence of the two BVs explains the behaviour of the wake field for $\beta \neq 0°$. Recalling the $\beta = 0°$ wake, it was dominated by the rotating flow in the two symmetric ABVs. However, one of them disappeared when $\beta \neq 0°$. The reason is that the oblique flow forces the port BV into the centreline wake, where the ABV is located. Since the two vortices are counter rotating their strengths will be reduced and the rotational flow in the port ABV disappears. On starboard side the BV is forced into the far field, which means that the interference with the ABV is weak. Furthermore the two vortices are co-rotating, which means that the BV may help driving the ABV leading to increased strength.

14.1.5. Pressure distribution for pure drift

Comparison of the cases $\beta = 0°$ and $\beta = 4°$, reveals strong port-starboard asymmetry, as shown in Figure 14.3 (b) and (f). On the port (windward) side of the hull the stagnation zone increases. The pressure around the fore body bilge decreases, which correlates with the high velocity region discussed

earlier. On starboard (leeward) side Figure 14.3 (a) and (e) show that the extent of the stagnation region is reduced. The shoulder pressure decreases, while the pressure on the fore body bilge slightly increases when the bilge flow is decelerated due to the oblique flow. Over the midship section the influence of the oblique flow on the pressure field is weak, as shown in Figure 14.3 (e) and (f). The bilge regions are an exception, since the BVs decrease the pressure. The effect is strongest on windward side and, according to bare hull data, it is more pronounced when the drift angle is increased beyond 4°. On leeward side, the pressure in the aft body bilge region and on the rear part of the stern decreases with increased drift angle. On windward side of the stern the pressure decrease slightly.

On the rudder itself, the pressure field is shown in more detail in Figure 14.9, in connection with the discussion of propeller effects on the local rudder pressures. As shown in Figures 14.3 and 14.9 the pressure varies in both chordwise and spanwise directions. In the chordwise direction on the starboard side, the pressure is high in the stagnation zone, with a peak on the upper part of the leading edge. Further downstream, the pressure decreases before it recovers again towards the trailing edge. In the spanwise direction the pressure is low on the lower half of the rudder, but it increases on the upper part. Compared to the rudder surface pressure for $\beta = 0°$ in Figure 14.3 (a), a general decrease is observed on the starboard side, which for $\beta = 4°$ acts as the suction side of the rudder. On the port side of the rudder, which acts as the pressure side, Figure 14.3 (f) and (b) show that the pressure increases. High pressure is located in the leading edge region of the rudder, with a peak at the tip, and the pressure decreases from the tip towards the root. The spanwise variation correlates with the inboard-directed flow at the upper part of the rudder, which increases the pressure at the top compared to the bottom.

14.2. Body forces, velocities and pressures with propeller

14.2.1. Axial velocities for straight-ahead and static rudder

The velocity, pressure and body force fields for the with-propeller conditions are documented in References /6/ and /9/, and briefly summarised herein.

The axial evolution of the velocity fields without propeller are described in Section 14.1. Figure 14.4 shows the contours of axial velocity and vorticity $\omega_X = \partial W / \partial y - \partial V / \partial z$ at the AP, $X/L_{PP} = 1.0$, for both with and without propeller conditions.

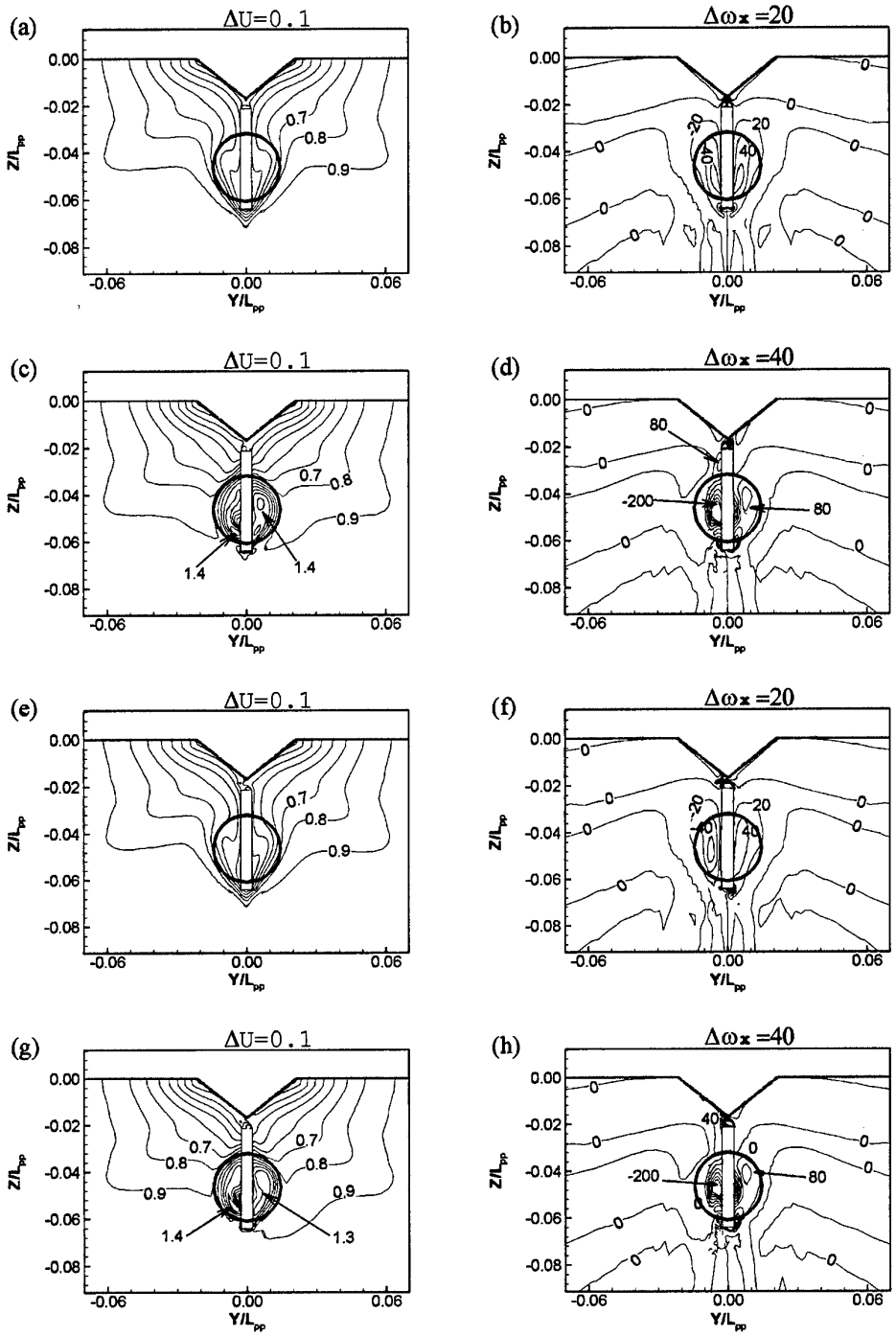

Figure 14.4 Axial velocity and vorticity at cross plane located at AP: (a) and (b), $\beta = \delta = 0°$, no propeller; (c) and (d), $\beta = \delta = 0°$, with propeller; (e) and (f), $\beta = 0°$, $\delta = -10°$, no propeller; (g) and (h), $\beta = 0°$, $\delta = -10°$, with propeller

The without-propeller condition, shown in Figure 14.4 (a) and (b), is covered in detail in Reference /8/, and summarised in Section 14.1. As noted therein a thin boundary layer builds up along the hull and thickens rapidly in the stern region of the hull. The flow is retarded over a relatively large portion of the wake region, so the rudder operates in an flow field where the axial velocity is less than half of the ship speed, as shown in Figure 14.4 (a). With respect to the cross flow, which here is represented by the axial

vorticity, Reference /8/ and Section 14.1 show that the flow in the propeller region is strongly dominated by the two inboard and counter rotating aft body bilge vortices (ABV), which are located symmetrically on each side of the centreplane of the ship, as shown in Figure 14.4 (b).

When the propeller is included in the simulation, the flow field changes. As shown in Figure 14.4 (c) and (a), the axial velocity in the outer wake field is quite similar to the case without propeller, but locally where the slipstream passes the rudder, the flow is accelerated to 1.4 times the ship speed. A low speed region is observed in the slipstream very close to the rudder. This region originates from the hub region, where the flow is not accelerated, since no body-forces are applied. Overall, the contours are no longer symmetric with respect to the centreplane, because the combination of the rotating propeller, the non-uniform axial inflow field and the two counter rotating ABV's leads to an asymmetrical propeller loading, shown in Figure 13.6, which again results in a asymmetrical velocity field. With respect to the effective local axial propeller force shown in Figure 13.6 (a) it is seen that the propeller works hardest in the top and the bottom of the disk, where the wake deficit is most pronounced. Further, the starboard side loading is higher then the port side loading for the same reasons as explained in connection with the Series 60 ship. The starboard/port differences correlate with axial velocity field, which shows that the flow is accelerated more on starboard side than on port side.

With respect to the cross flow, the two ABVs are still present when the propeller is turned on, but the strength and the position of the vortices change. On port side of the part of the rudder in the slipstream the vortex moves slightly downward and closer to the rudder. Further, the strength increases, because the hub vortex behind the propeller apparently helps driving the flow in the port ABV vortex. On the starboard side of the part of the rudder in the slipstream, the vortex moves upwards and away from the rudder and at the same time, the strength increases. Close to the rudder above the slipstream, the axial vorticity also changes and the sign change of the vorticity indicates, that the fluid now moves upwards instead of downwards. On the port side this behaviour is explained by the fact that the propeller swirl directs the fluid towards the rudder surface. When the fluid hits the surface, a part of it will be forced upwards, while another part will be forced downwards. On starboard side, the swirl, which is going in the opposite direction of the bilge vortex flow, deflects the bilge vortex flow in a way so the parts of it are forced upwards.

When the rudder is turned to $\delta = -10^\circ$ without the propeller, the stern flow looses its centreplane symmetry, as discussed in Section 14.1. When the propeller is turned on, with a deflected rudder, the outer contours appear to be more effected than for zero rudder angle, since the port side contours move upwards while the starboard side contours move downwards because of the propeller rotation, as shown in Figure 14.4 (g) and (c). In the propeller slipstream the flow is still accelerated, but the magnitude of the velocity follows the trend from the without-propeller case. This means that the velocity increases on port side, while it decreases on starboard side. Further the hub-generated low velocity region can still be seen.

The effect of the turned rudder on the axial body forces can be seen from a comparison between the effective force field in 13.6 (a) and the static rudder field in 14.5 (a). On the port side, the load is approximately the same, but on the starboard side it has increased. The reason is that the propeller inflow field on this side is retarded due to stagnation on the pressure side of the rudder, increasing the propeller loading.

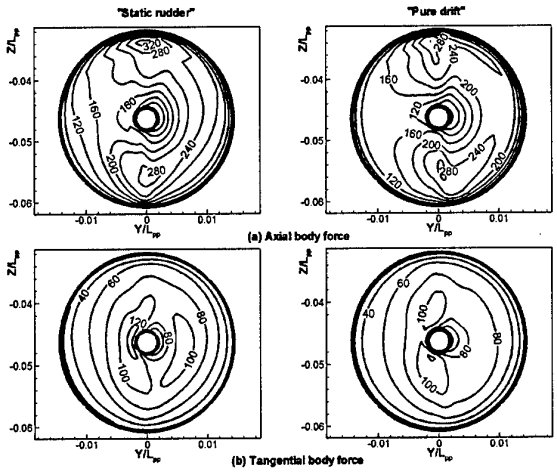

Figure 14.5 Axial and tangential body forces for static rudder and pure drift

Concerning the cross flow, a comparison between Figure 14.4 (h) and (d) shows approximately the same overall pattern of the contours. Though differences are observed, since the axial vorticity slightly increases and decreases in the slipstream region on port and starboard sides, respectively. Finally, the tangential body-force component for the static rudder field in Figure 14.5 (b) shows that the propeller loading is higher in the vicinity of the hub than was the case for the zero rudder angle condition.

14.2.2. Pressure and streamlines for straight-ahead and pure rudder

Detailed views of the pressure distributions on the rudder and the stern of the ship for straight-ahead and static rudder are plotted in Figure 14.6 and Figure 14.7, together with the limiting streamlines. Starting with $\beta = 0°$, $\delta = 0°$, Figure 14.6 (a) and (b) show the without-propeller condition on port and starboard sides, respectively.

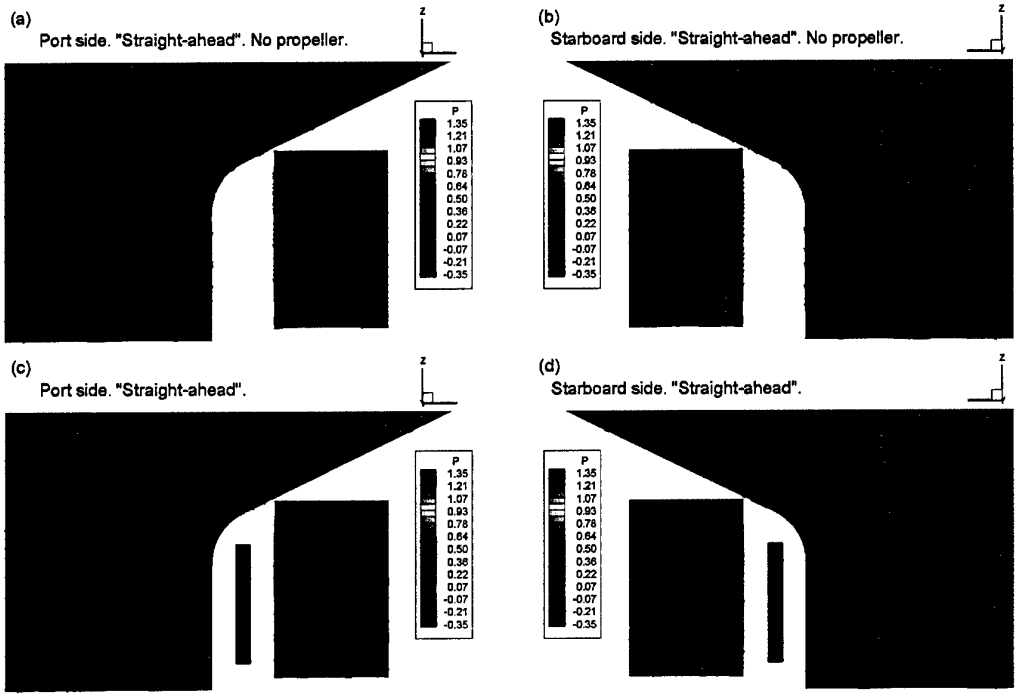

Figure 14.6 Pressure distribution and limiting streamlines on stern region. (a) and (b) straight-ahead without propeller. (c) and (d) straight-ahead with propeller

The pressure field for the straight ahead and static rudder conditions, without propeller, are described in detail in Reference /8/ and summarised in Section 14.1. When the propeller is turned on the pressure field changes. On the hull, the suction on the hull from the propeller is reflected in a decrease of the pressure in the region in front of the propeller. The suction can also be seen in the streamline pattern, since the zones with re-circulating flow on the lower part of the hull disappear. On the rudder itself, the increase in the axial velocity over the part of the rudder in the propeller slipstream decreases the pressure. The swirl in the propeller slipstream can also be seen in the pressure field. For instance in the upper part of the slipstream on the port side of the leading edge a high-pressure region is observed. This region occurs when the swirl hits the rudder surface. On the opposite side of the rudder a low-pressure region occurs, due to a "shadow" effect of the rudder. In the lower part of the slipstream, the opposite happens, due to the rotation of the propeller. With respect to the streamlines on the rudder, the streamlines in the slipstream diverge in the region where the swirl hits the rudder, whereas in the regions with "shadow" they converge. Outside the propeller slipstream, i.e. in the upper part of the rudder, the streamlines change direction, since they now point upward instead of downward. This correlates with the findings for the axial vorticity described above.

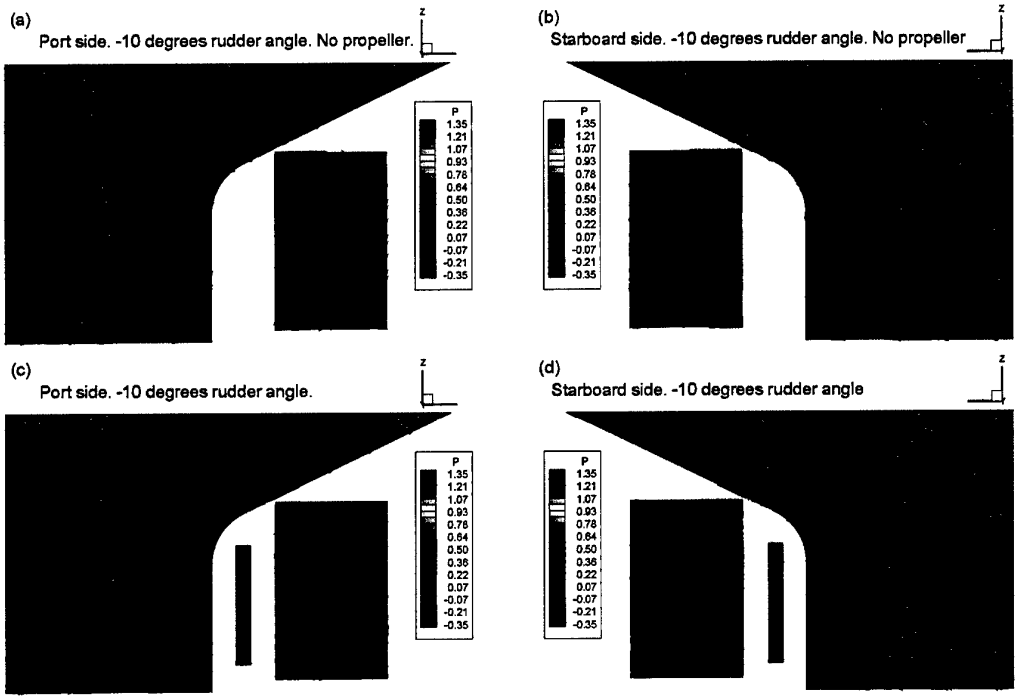

Figure 14.7. Pressure distribution and limiting streamlines on stern region. (a) and (b) static rudder without propeller. (c) and (d) static rudder with propeller

With the rudder deflected –10°, and the propeller included, the flow patterns in Figure 14.7 (c) and (d) develop. The suction on the hull can again be seen as decreasing hull pressure and reduced back flow. If the zero rudder angle and the deflected rudder cases are compared, it is seen that the overall behaviour is the same as observed without propeller. This means that the port side pressure generally decreases, while the starboard side pressure increases. Further, the pressure peaks caused by the swirl hitting the rudder surface can also be seen. The streamline pattern further reveals the rudder tip effects, which are more pronounced with the rudder deflected. On the starboard side, the flow is clearly deflected towards the tips due to the suction on the other side of the rudder. On the port side the tip vortex can clearly be seen at the very lowest part of the rudder, where the propeller actually helps drive the vortex. At the root no vortex is present, due to the fact that the propeller forces the water towards the root and prevents the vortex from developing. Finally, the zone with reversed flow, which was seen without the propeller, is still present, but it has moved slightly in the upward and upstream directions.

14.2.3. Velocities and body forces for pure drift

A detailed explanation of the flow pattern for the pure drift condition, without propeller, is given in Reference /8/ and summarised in Section 14.1. Figure 14.8 (a) and (b) show the axial velocity and vorticity contours at $X/L_{PP} = 1.0$ for the condition, $\beta = 4°$ and $\delta = 0°$, without propeller. Figure 14.8 (c) and (d) show the axial velocity and vorticity contours with the propeller included. Outside the propeller slipstream the change in the axial velocity is relatively weak, but it should be noticed that the hook shape of the outer contours on port side is less pronounced than without the propeller. Inside the propeller slipstream, the maximum magnitude of the axial velocity component is the same as in the straight-ahead case, but the distribution of the contours is slightly different, since the propeller is in a different inflow field. The change in the propeller loading is seen in Figure 13.6 (a) and Figure 14.5 (a). Due to the higher inflow velocity on the port side, the propeller is more lightly loaded on this side. On the starboard side it is a more difficult to say if the propeller loading overall is higher or lower than for straight-ahead, but the differences can be seen in the figures. With respect to the cross flow in 14.8 (d) it is seen that the extent of the high vorticity region on the port side of the rudder is reduced compared to straight-ahead, whereas on the starboard side, the vorticity increases. According to Reference /8/ the explanation is to be found in

the fact that the strengths of the ABVs change due to interference with another set of vortices (BV) coming from the bilges further upstream. With respect to the tangential body-force component it mainly shows changes in the region close to the hub, where the force increases.

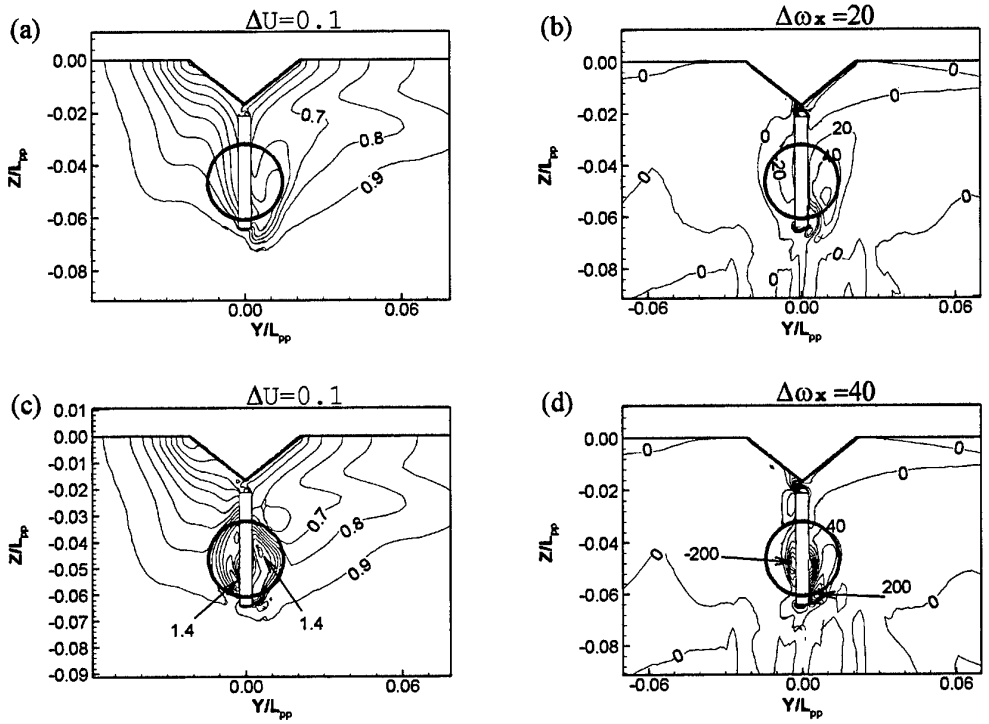

Figure 14.8 Axial velocity and vorticity at cross plane located at AP. (a) and (b), $\beta = 4°$ and $\delta = 0°$, no propeller. (c) and (d), $\beta = 4°$ and $\delta = 0°$, with propeller.

14.2.4. Pressures and streamlines for pure drift

The pressure distribution and limiting streamlines for the pure drift condition are shown in Figure 14.9. The without-propeller condition on port and starboard sides can be seen in Figure 14.9 (a) and (b), respectively. The pressure and streamlines are described in detail in Reference /8/ and summarised in Section 14.1. The pressure field and streamlines with propeller operating are shown in Figure 14. 9 (c) and (d). On the hull, the pressure decreases due to the suction of the propeller. The suction can also be seen in the streamline pattern, since the zones with re-circulating flow either are reduced or completely gone. On the rudder the pressure reveals the swirl generated peak regions close to the leading edges plus low-pressure regions due to flow acceleration in the propeller slipstream. Concerning the rudder streamline pattern, the streamlines in the slipstream diverge where the swirl hits the rudder, while they converge in the corresponding regions on the opposite side of the rudder. Further, diverging streamlines are also observed on the upper part of the rudder outside the slipstream. It is most pronounced on port side, since the fluid moves towards the rudder tip in or to flow to the low-pressure suction or leeward side. Finally, the small re-circulating zone, which was observed before the propeller was turned on, disappears.

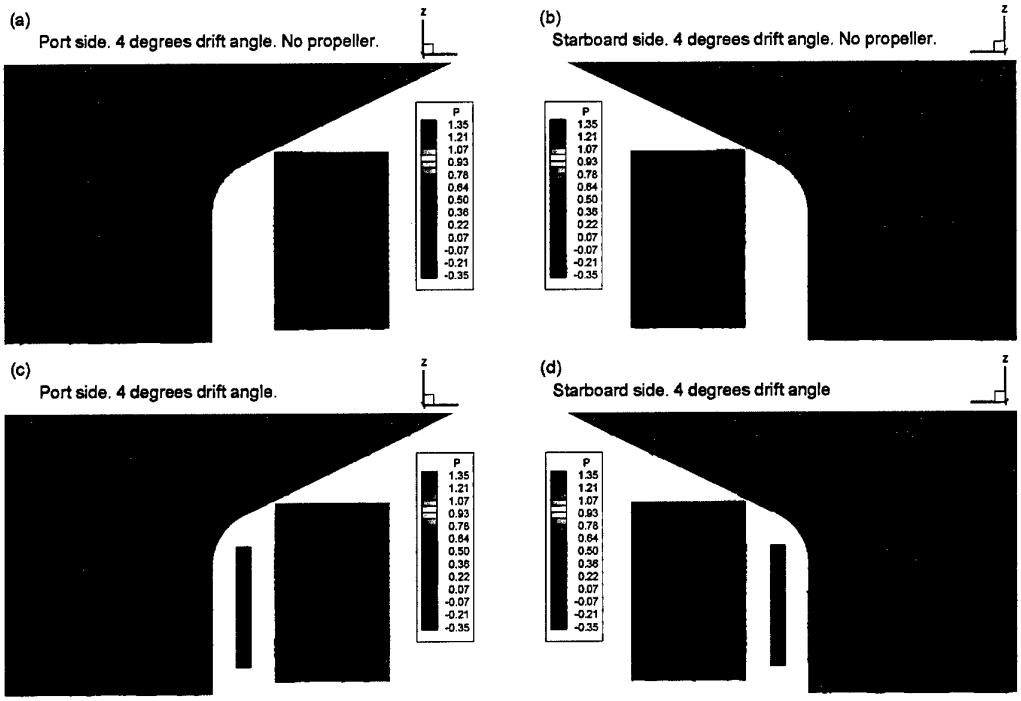

Figure 14.9. Pressure distribution and limiting streamlines on stern region. (a) and (b) pure drift without propeller. (c) and (d) pure drift with propeller.

15. Dissemination

During the course of the project a series of technical papers, References /3/ through /9/, have been prepared, covering different aspects of the work covered.

References /5/ and /6/ have been presented at international workshops. References /7/ and /9/ are to appear, and Reference /8/ is to be presented at an international conference.

16. References

/1/ *Proposal: Development and Validation of Computational Ship Hydrodynamics*, Danish Maritime Institute, 2000.

/2/ Simonsen C. D., *Rudder, Propeller and Hull Interaction by RANS*, Ph.D. thesis, The Technical University of Denmark, 2000

/3/ Arnskov, Cross-Whiter, J., Simonsen C., *Fiscal Year 2001 Annual Report*, ONR Grant N00014-00-1-0589, 2001

/4/ Cross-Whiter, J.,Simonsen C., *Fiscal Year 2002 Annual Report*, ONR Grant N00014-00-1-0589, 2002

/5/ Simonsen, C.D. and Cross-Whiter, J. , "RANS Simulation of the Flow around Manoeuvring Tanker", 4th Numerical Towing Tank Symposium, 2001

/6/ Simonsen, C.D. and Cross-Whiter, J. "Study of three RANS body-force propeller models," 5th Numerical Towing Tank Symposium, Pornichet, France, 2002

/7/ Simonsen, C.D. and Stern F. "Verification and validation of RANS maneuvering simulations of Esso Osaka: effects of drift and rudder", *Computers & Fluids*, to appear

/8/ Simonsen C.D. and Stern F., "Flow structure around an appended tanker hull form in simple maneuvering conditions", The 8th International Conference on Numerical Ship Hydrodynamics, September 22-25, 2003, Busan Korea

/9/ Simonsen, C.D. and Stern, F., "RANS maneuvering simulation of Esso Osaka with rudder and a body-force propeller", *Journal of Ship Research*, to appear

/10/ Stern, F., Kim, H. T., Zhang, D. H., Toda, Y., Kerwin, J. and Jessup S., "Computation of Viscous Flow Around Propeller-Body Configurations: Series 60 C_B =0.6 Ship Model", *Journal of Ship Research*, Vol. 38, No. 2, June. 1994

/11/ Yamasaki, R., "On the propulsion Theory of Ships on Still Water-Introduction," Memoirs of the Faculty of Engineering, Kyushu University, Vol. 27 No. 4, 1968

/12/ Nakatake, K. "A Practical Method to Calculate Propulsive Performance of Ships," Memoirs of the Faculty of Engineering, Kyushu University, Vol. 41 No. 1, 1981

/13/ Hsin, C-Y, *Development and Analysis of Panel methods for Propellers in Unsteady Flow*, Report 91-1, Massachusetts Institute of Technology, 1991

/14/ Black, SD, *Integrated Lifting-Surface/Navier-Stokes Design and Analysis Methods for Marine Propellers*, Ph.D. Thesis, Massachusetts Institute of Technology, 1997.

/15/ Toda, Y. Stern, F., Tanaka, I. and Patel, V. C., "Mean-flow measurements in the boundary layer and wake of a Series 60 C_B=.6 model ship with and without propeller" *Journal of Ship Research*, Vol. 34, No. 4, 1990